

Networked Sensing with AI-Empowered Interference Management: Exploiting Macro-Diversity and Array Gain in Perceptive Mobile Networks

Lei Xie and Shenghui Song

Abstract

Sensing will be an important service for future wireless networks to assist innovative applications like autonomous driving and environment monitoring. Perceptive mobile networks (PMNs) were proposed to add sensing capability to current cellular networks. Different from traditional radar, the cellular structure of PMNs offers multiple perspectives to sense the same target, but the inherent interference between sensing and communication and the joint processing among distributed sensing nodes (SNs) cause big challenges for the design of PMNs. In this paper, we first propose a two-stage protocol to tackle the interference between two sub-systems. Specifically, the echoes created by communication signals, i.e., interference for sensing, are first estimated in the clutter estimation (CE) stage, which are then utilized for interference management in the target sensing (TS) stage. A *networked* sensing detector is then derived to exploit the perspectives provided by multiple SNs for sensing the same target. The macro-diversity from multiple SNs and the array gain from multiple receive antennas at each SN are investigated to reveal the benefit of networked sensing. Furthermore, we derive the sufficient condition that one SN's contribution to networked sensing is positive, based on which a SN selection algorithm is proposed. To reduce the computation and communication workload, we propose a model-driven deep-learning algorithm that utilizes partially-sampled data for CE. Simulation results confirm the benefits of networked sensing and validate the higher efficiency of the proposed CE algorithm than existing methods.

Index Terms

L. Xie and S. Song are with Department of Electronic and Computer Engineering, the Hong Kong University of Science and Technology, Hong Kong. e-mail: ({eelxie, eeshsong}@ust.hk).

Perceptive mobile network, integrated sensing and communication, macro-diversity, array gain, unfolding deep networks.

I. INTRODUCTION

With the development of innovative applications such as autonomous driving and industrial internet of things (IIoT) [1]–[3], there is an increasing demand on sensing services such as target tracking and environmental monitoring [4], [5]. Unfortunately, the current mobile networks, though very successful in providing communication services, are not able to meet the accurate sensing requirement of the above applications. To this end, the recently proposed integrated sensing and communication (ISAC) provides a promising platform to integrate sensing with wireless communication [6], [7], where the adoption of millimeter wave (mmWave) by 5G and beyond systems further enables the hardware and software reuse between two systems. As a special type of ISAC system, perceptive mobile networks (PMNs) were proposed to add sensing ability to current cellular networks [5], [8].

There are many favorable properties of mobile networks that can facilitate sensing. First, the well developed cellular networks can provide large surveillance coverage. Second, the high-density and multiple-antenna sensing nodes (SNs), such as base stations (BSs), not only offer sufficient spatial freedom for interference cancellation, but also enables networked sensing. Finally, the strong computation and communication power of the network provides a good platform to estimate the echoes created by communication signals, such that the interference from communication to sensing can be properly tackled. This process is called clutter¹ estimation (CE), which is critical for radar sensing, especially with complex environment. However, there are also new challenges. For example, the integration of sensing and communication requires proper interference management between the two systems in both device (full-duplex operation [9]) and network level (multi-user interference [10]). On the one hand, the newly added sensing signals should avoid generating interference to existing communication users. On the other hand, the interference from communication to sensing, represented by the clutter caused by communication signals should also be well handled. Finally, the networked sensing with distributed nodes may cause heavy communication and computation workload over the network and faces stringent latency requirement.

¹The echoes backscattered from the clutter patches, including the communication users and their nearby scatter points, are referred to as the clutter [16], [17].

Interference management is at the core of ISAC network design. In the device level, utilizing BSs to serve communication users and sense targets at the same time will cause self-interference and require full-duplex operation. Some research efforts have been made on self-interference cancellation (SIC) [11], [12] to enable full-duplex operation, which unfortunately is still not very mature. [5] addressed the full-duplex issue by separating the sensing transmitter and receiver to different remote radio units (RRUs) in a cloud radio access network (C-RAN). Along the same line of research, [15] proposed to utilize another layer of passive target monitoring terminals (TMTs) to save the need for full-duplex operation. However, the networked sensing that can exploit the perspectives from multiple SNs, e.g., BSs, RRUs, UAVs, or TMTs, has not been well investigated.

In the network level, there is inherent interference between sensing and communication. In particular, in PMNs, communication signals will create the clutter for sensing, representing the interference from communication to sensing. Estimation of the clutter is very critical for accurate sensing. The authors of [18] proposed to construct clutter based on the estimated sensing parameters, e.g., time delay, Doppler frequency and direction, and then remove it from the signal. However, the computational cost of the compressed sensing (CS)-based parameter estimation can be extremely high due to the continuous and rapidly-changing clutter parameters in the space and Doppler domains. This issue will be more serious for networked sensing where information sharing between multiple SNs are necessary. Thus, a computation and communication efficient CE algorithm is desired.

In this paper, we will investigate networked sensing and its associated CE. These two issues are similar for PMNs with different SNs, e.g., BSs, RRUs, UAVs, or TMTs. Here, we consider the PMN with distributed TMTs and the results can be applied to PMNs with other SNs. TMTs are passive nodes with only perception functionalities, including radar, vision, and other sensing capabilities [3], [19]. They are distributed in a target area and connected with the data center on the base stations (BSs) through low latency links. As a result, BSs will serve as radar transmitters besides performing their communication duty and the sensing task is jointly performed by TMTs to avoid full-duplex operation.

We first propose a two-stage protocol where CE and TS are performed in two consecutive periods, respectively, where the clutter created by communication signals will be estimated in the CE period and then utilized for TS. Furthermore, in order to guarantee the clutter statistics donot change in the TS period, the sensing signal is properly designed to avoid affecting the

clutter. We then derive a networked detector based on the generalized likelihood ratio test (GLRT) detection, which is optimal in terms of maximizing the signal-to-clutter-plus-noise ratio (SCNR). Performance analysis reveals the impact of several key system parameters, including the number of TMTs and the number of antennas at the TMT. Physical insights with respect to the macro-diversity and array gain are then revealed, identifying the unique advantages of networked sensing.

To reduce the computation and communication workload for CE, we further propose a distributed clutter covariance estimation algorithm where the estimation is performed at TMTs. The low rank clutter in mmWave channel [20]–[22] makes it possible to estimate the clutter covariance by using partial samples of the received signal. However, the estimated covariance matrix may be ill-conditioned due to the limited data samples. To this end, we unfold the expectation-maximization (EM) detector with several learnable parameters and propose the EM-Net algorithm, which achieves accurate estimation with less data than existing methods.

The contributions of this paper can be summarized as follows:

- 1) We propose a two-stage protocol for sensing the target in PMNs in the presence of clutter. First, the clutter created by communication signals is estimated in the CE stage, whose results are utilized for interference management in the TS stage. To ensure the clutter in the signal-under-test has the same statistical structure as the estimated one from CE, the precoder for sensing signal is designed not to affect the clutter patches in the TS stage.
- 2) We derive a networked detector where multiple TMTs collaboratively sense a target with a constant false alarm probability. We theoretically evaluate the performance of the proposed detector, whose accuracy is validated by simulation.
- 3) The impact of the number of TMTs and the number of antennas at the TMTs are investigated. For the former, we derive the sufficient condition for the contribution of one TMT to be positive and propose a TMT selection algorithm based on the condition. For the latter, we show that, different from communication, multiple antennas only provide array gain but no diversity gain for the considered detection problem, due to the use of only the line-of-sight (LoS) component. Note that multiple antennas do offer more degrees of freedom for sensing. For example, they can improve angular resolution [23], [24].
- 4) To improve the computation and communication efficiency, we propose an efficient CE method by unfolding the EM algorithm where several learnable parameters are introduced. Compared with the existing method, the proposed algorithm can achieve better estimation

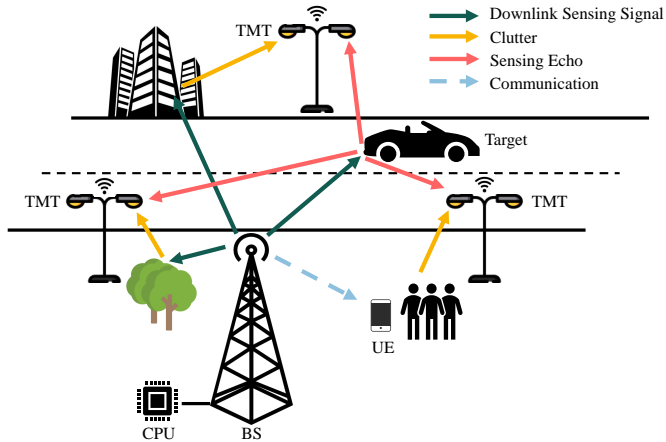


Fig. 1. Illustration of system structure.

performance with less data samples.

The remainder of this paper is organized as follows. Section II introduces the system model and the two-stage protocol. The networked detector is derived in Section III where its performance evaluation is also given. Based on the analysis results, the impact of several key parameters, including the number of TMTs (macro-diversity) and the number of antennas (array gain) are also investigated. An unfolded EM algorithm is proposed in Section IV for efficient CE. Section V validates the performance of the proposed networked detector and the efficiency of the proposed CE algorithm by simulation. Finally, Section VI concludes this paper.

II. SYSTEM MODEL AND TWO-STAGE SENSING

Consider a PMN where passive TMTs are deployed over conventional cellular networks for sensing purposes, as illustrated in Fig. 1. Assume that the BSs and TMTs are equipped with N_T and N_R antennas, respectively. All the TMTs are connected with the data center on the base stations (BSs) through low latency links to achieve the clock synchronization, which is an inherent challenge for networked sensing due to the distributed nature of the network [9]. The objective in this paper is to detect whether a target is present at a given location. Note that the adding of the TMTs saves the need for full-duplex operation, while the protocol and algorithms proposed in this paper are valid for other PMN architectures, such as those using full-duplex BSs and RRUs as the SNs. The target is assumed to be point-like and static or slow-moving, which is also known as the Swerling I model [25], where the Doppler effect is neglected. The target detection problem is formulated as a hypothesis testing between \mathcal{H}_0 (target absence) and

\mathcal{H}_1 (target presence) and achieved by a likelihood ratio test [16], [17]. The decision statistic requires the statistical information of the clutter to construct the probability density function for both the clutter-alone case (\mathcal{H}_0) and the signal-plus-clutter case (\mathcal{H}_1).

To achieve the detection in PMN system, we propose a two-stage protocol as illustrated in Fig. 2. Note that the normal communication service is not affected by sensing, which only happens in the downlink time. In particular, the downlink time is divided into two periods, i.e., the CE period and TS period. During the CE period, BSs only serve the communication users, while the radar detection is jointly achieved by multiple TMTs in the TS period. In the following, we explain the detailed operations of the two periods, respectively.

A. Communication and CE Period

In this period, the BSs will send communication signals to the UEs, which will be reflected by the clutter patches and captured by TMTs for CE. In this paper, we consider the target that is not very close to the UEs. Thus, due to the narrow beam in the mmwave system, the echo reflected from the target can be ignored². Specifically, in the n th subframe, the BS transmits communication signals to K UEs and the received signal at the l th TMT is given as [28], [29]

$$\mathbf{y}_{c,l}(n) = \mathbf{H}_l(n)\mathbf{F}\mathbf{s}(n) + \mathbf{n}_l(n), n = 1, 2, \dots, N, \quad (1)$$

where $\mathbf{s}(n) \in \mathbb{C}^{K \times 1}$ denotes the communication symbol with covariance matrix \mathbf{I} , $\mathbf{F} \in \mathbb{C}^{N_T \times K}$ represents the precoder matrix, which can be designed according to the communication requirement based on some existing methods, e.g., the maximal-ratio combining [30] and zero-forcing [31], and $\mathbf{n}_l(n)$ is the additive white Gaussian noise (AWGN) with zero mean and covariance matrix $\sigma^2\mathbf{I}$. Note that $\mathbf{F}\mathbf{s}(n)$ and $\mathbf{y}_{c,l}(n)$ correspond to the ‘‘Communication Signal’’ and ‘‘Clutter Echo’’ in Fig. 2, respectively.

Here, $\mathbf{H}_l(n) \in \mathbb{C}^{N_R \times N_T}$ denotes the channel matrix between the BS and the l th TMT. With uniform linear array, the steering vector of the BS with angle of departure (AOD) ϕ and that of the l th TMT with angle of arrive (AOA) θ are respectively defined as

$$\mathbf{a}_T(\phi) = \frac{1}{\sqrt{N_T}} \left[1, e^{j2\pi \frac{d}{\lambda} \cos \phi}, \dots, e^{j2\pi(N_T-1)\frac{d}{\lambda} \cos \phi} \right]^T \in \mathbb{C}^{N_T \times 1}, \quad (2)$$

²Otherwise, if the echo is not negligible, the effect of the target echo can be alleviated by removing the target signal component from the estimated covariance matrix [26] or selecting the target-free data through training sample censoring [27].

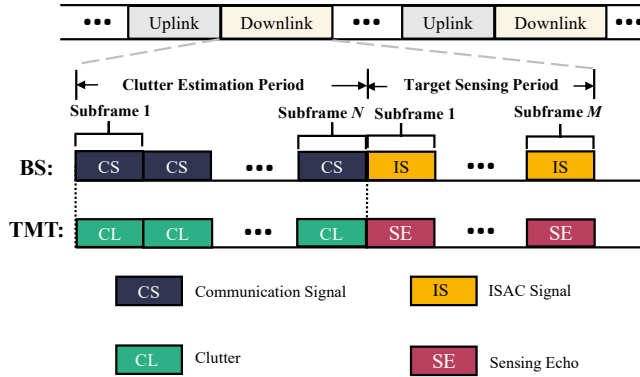


Fig. 2. Frame structure for the proposed integrated sensing and communication protocol.

$$\mathbf{a}_R(\theta) = \frac{1}{\sqrt{N_R}} \left[1, e^{j2\pi \frac{d}{\lambda} \cos \theta}, \dots, e^{j2\pi (N_R-1) \frac{d}{\lambda} \cos \theta} \right]^T \in \mathbb{C}^{N_R \times 1}, \quad (3)$$

where d is the antenna spacing and λ represents the wave length. Thus, the channel matrix with P clutter patches is defined as

$$\mathbf{H}_l(n) = \sqrt{N_R N_T} \sum_{i=1}^P \epsilon_{l,i}(n) \mathbf{a}_R(\theta_{l,i}) \mathbf{a}_T^H(\phi_i) \in \mathbb{C}^{N_R \times N_T}, \quad (4)$$

where $\epsilon_{l,i}(n)$ denotes the reflecting coefficient of the i th clutter patch observed by the l th TMT, which is assumed to follow a complex Gaussian distribution with zero mean and variance $\sigma_{l,i}^2$ [32]. ϕ_i denotes the AOD of the i th clutter patch from the BS and $\theta_{l,i}$ represents the AOA of the i th clutter patch to the l th TMT. Here, we omit the paths reflected more than one time. These P clutter patches come from two sources: 1) the UEs, and 2) the strong scatter points near UEs. Note that the reflecting coefficient of the UEs may be low, but the transmit power towards the UEs is high. Therefore, the echoes from the UEs can not be neglected. Note that $\mathbf{y}_{c,l}(n), n = 1, 2, \dots, N$ are independent and identically distributed (i.i.d) with respect to n , due to the i.i.d., communication signals.

For ease of illustration, we rewrite (1) as

$$\mathbf{y}_{c,l}(n) = \mathbf{A}_{R,l} \mathbf{t}_l(n) + \mathbf{n}_l(n), n = 1, 2, \dots, N, \quad (5)$$

where

$$\mathbf{A}_{R,l} = [\mathbf{a}_R(\theta_{l,1}), \dots, \mathbf{a}_R(\theta_{l,P})] \in \mathbb{C}^{N_R \times P},$$

$$\mathbf{t}_l(n) = \left[\sqrt{N_R N_T} \epsilon_{l,1}(n) \mathbf{a}_T^H(\phi_1) \mathbf{F} \mathbf{s}(n), \dots, \sqrt{N_R N_T} \epsilon_{l,P}(n) \mathbf{a}_T^H(\phi_P) \mathbf{F} \mathbf{s}(n) \right]^T \in \mathbb{C}^{P \times 1}.$$

Note that the instantaneous value of the reflecting coefficient can change with the different frames, while the statistical information of the reflecting coefficient remains constant. Therefore, $\mathbf{y}_{c,l}(n)$ follows the Gaussian distribution with $\mathbf{y}_{c,l}(n) \sim \mathcal{CN}(\mathbf{0}, \mathbf{R}_{c,l})$ for $n = 1, \dots, N$, where

$$\mathbf{R}_{c,l} \triangleq \mathbb{E} \{ \mathbf{y}_{c,l}(n) \mathbf{y}_{c,l}^H(n) \} = \underbrace{\mathbf{A}_{R,l} \mathbf{P}_l \mathbf{A}_{R,l}^H}_{\text{Clutter}} + \underbrace{\sigma^2 \mathbf{I}}_{\text{Noise}}, \quad (6)$$

and

$$\mathbf{P}_l = \text{Diag} \left(\left[\sqrt{N_R N_T} \sigma_{l,1}^2 |\mathbf{a}_T^H(\phi_1) \mathbf{F}|^2, \dots, \sqrt{N_R N_T} \sigma_{l,P}^2 |\mathbf{a}_T^H(\phi_P) \mathbf{F}|^2 \right] \right). \quad (7)$$

The main task of the TMTs in this period is to estimate the clutter covariance matrix $\mathbf{R}_{c,l}$ based on the received signal $\mathbf{y}_{c,l}(n)$, $n = 1, \dots, N$.

B. Communication and TS Period

In the TS period, the system aims to probe a target without influencing the communication performance. To achieve good sensing performance, the received clutter in the TS period is supposed to have the same second-order statistics as that in the CE period. For that purpose, we need to properly design the precoder to avoid affecting the covariance structure of the clutter in the TS period. Assume the channel information between the BS and UEs, i.e., $\{\phi_i\}_{i=1}^P$ are known from channel estimation of the communication systems. To make sure the second order statistics of the echo signals do not change in the TS period, we need to guarantee that the sensing signal toward the ST, with AoD ϕ_t , will not create echoes by the clutter patches³. For that purpose, we define

$$\mathbf{A}_T = [\mathbf{a}_T(\phi_1), \dots, \mathbf{a}_T(\phi_P)] \quad (8)$$

and construct \mathbf{f}_\perp as the projection of $\mathbf{a}_T(\phi_t)$ in the null-space of \mathbf{A}_T , i.e.,

$$\mathbf{f}_\perp = \frac{\mathbf{a}_T(\phi_t) - \mathbf{A}_T (\mathbf{A}_T^H \mathbf{A}_T)^{-1} \mathbf{A}_T^H \mathbf{a}_T(\phi_t)}{1 - \mathbf{a}_T^H(\phi_t) \mathbf{A}_T (\mathbf{A}_T^H \mathbf{A}_T)^{-1} \mathbf{A}_T^H \mathbf{a}_T(\phi_t)}. \quad (9)$$

It can be validated that $\mathbf{A}_T^H \mathbf{f}_\perp = \mathbf{0}$, i.e., \mathbf{f}_\perp will not affect the response on the direction of clutter patches. It has been shown in [15] that redesigning communication signals for sensing is more efficient than creating a dedicated sensing signal. Thus, we design the precoder and symbols in the TS period as

$$\mathbf{F}_{\text{ISAC}} = \mathbf{F} + \mathbf{f}_\perp \boldsymbol{\omega}^T, \quad (10)$$

³We assume that $\phi_t \neq \phi_i, \forall i$, because otherwise the target can not be detected.

where $\boldsymbol{\omega} = [\omega_1, \omega_2, \dots, \omega_K]^T$ denotes the weights for the data streams of K UEs⁴. Here, $\mathbf{F}_{\text{ISACS}} = \mathbf{F}\mathbf{s} + \mathbf{f}_\perp \boldsymbol{\omega}^T \mathbf{s}$ corresponds to the ‘‘ISAC Signal’’ in Fig. 2. Note that, compared with the transmit signal in the CE period, the additional signal $\mathbf{f}_\perp \boldsymbol{\omega}^T \mathbf{s}$ will not create echos from the clutter patches, including the UEs. This guarantees that the communication performance will not be affected by sensing and the clutter covariance structure is the same in the CE and TS periods.

For ease of illustration, we only consider one subframe in the TS period and the result can be extended to the case with more subframes. In this case, the received signal at the l th TMT in the TS period can be given by

$$\begin{aligned} \mathbf{y}_l &= \left(\sqrt{N_R N_T} \epsilon_{t,l} \mathbf{a}_R(\theta_{t,l}) \mathbf{a}_T^H(\phi_t) + \mathbf{H}_l \right) \mathbf{F}_{\text{ISACS}} + \mathbf{n}_l \\ &= c_{t,l} \mathbf{a}_R(\theta_{t,l}) + \mathbf{A}_{R,l} \mathbf{t}_l + \mathbf{n}_l, \end{aligned} \quad (11)$$

where $\theta_{t,l}$ denotes the AOA of the target at the l th TMT, and

$$c_{t,l} = \sqrt{N_R N_T} \epsilon_{t,l} \mathbf{a}_T^H(\phi_t) \mathbf{F}_{\text{ISACS}} = \sqrt{N_R N_T} \epsilon_{t,l} \left(\mathbf{a}_T^H(\phi_t) \mathbf{F} \mathbf{s} + \sum_{k=1}^K \omega_k s_k \right), \quad (12)$$

represents the complex amplitude of the target component with $\epsilon_{t,l}$ denoting the channel coefficient of the BS-target-TMT (l th) link. We assume that $\epsilon_{t,l}$ does not change in one TS subframe. Note that \mathbf{y}_l corresponds to the ‘‘Sensing Echo’’ in Fig. 2 and the first term in (11) represents the echo from the target.

According to (11), \mathbf{y}_l follows the Gaussian distribution with $\mathbf{y}_l \sim \mathcal{CN}(c_{t,l} \mathbf{a}_R(\theta_{t,l}), \mathbf{R}_l)$, where

$$\mathbf{R}_l \triangleq \mathbb{E} \left\{ (\mathbf{y}_l - c_{t,l} \mathbf{a}_R(\theta_{t,l})) (\mathbf{y}_l - c_{t,l} \mathbf{a}_R(\theta_{t,l}))^H \right\} = \mathbf{A}_{R,l} \mathbf{P}_l \mathbf{A}_{R,l}^H + \sigma^2 \mathbf{I}. \quad (13)$$

Note that the expectation operations in (6) and (13) are implemented over a whole frame. Comparing (6) and (13), we can observe that the clutter in the TS period has the same covariance matrix as that in the CE period. Without loss of generality, we denote $\mathbf{R}_{c,l} = \mathbf{R}_l$.

III. NETWORKED SENSING WITH MULTIPLE TMTS

The distributed TMTs provide multiple perspectives to observe the target. In this section, we propose a networked detector and then evaluate its performance to reveal some physical insights.

⁴In general, $\boldsymbol{\omega}$ can be determined based on the relation between the direction of target and UEs. Compared with forming a dedicated sensing data stream, the power transmitted to the target by reusing the communication signal is higher [15].

A. Networked Sensing

Radar detection is a binary hypothesis testing problem, where hypotheses \mathcal{H}_0 and \mathcal{H}_1 correspond to the absence and presence of the target, respectively, i.e.,

$$\begin{aligned}\mathcal{H}_0 : \mathbf{y}_l &\sim \mathcal{CN}(\mathbf{0}, \mathbf{R}_l) \\ \mathcal{H}_1 : \mathbf{y}_l &\sim \mathcal{CN}(c_{t,l}\mathbf{a}_R(\theta_{t,l}), \mathbf{R}_l)\end{aligned}\quad (14)$$

with \mathbf{y}_l denoting the signal-under-test at the l th TMT in the TS period. The conditional probability density function (pdf) of \mathbf{y}_l under two hypotheses are given by

$$\begin{aligned}f(\mathbf{y}_l|\mathcal{H}_0) &= C_N \det(\mathbf{R}_l)^{-1} \exp(-\mathbf{y}_l^H \mathbf{R}_l^{-1} \mathbf{y}_l), \\ f(\mathbf{y}_l; c_{t,l}|\mathcal{H}_1) &= C_N \det(\mathbf{R}_l)^{-1} \exp(-(\mathbf{y}_l - c_{t,l}\mathbf{a}_R(\theta_{t,l}))^H \mathbf{R}_l^{-1} (\mathbf{y}_l - c_{t,l}\mathbf{a}_R(\theta_{t,l}))),\end{aligned}\quad (15)$$

where C_N is a normalization coefficient. Given the echo signals received by different TMTs are independent due to the independent reflecting coefficients, the optimal detector that maximizes the output signal-to-clutter-plus-noise ratio (SCNR) is the generalized likelihood ratio test (GLRT) detector [33], i.e.,

$$\Delta_L = \frac{\max_{\{c_{t,l}\}} \prod_{l=1}^L f(\mathbf{y}_l; c_{t,l}|\mathcal{H}_1)}{\prod_{l=1}^L f(\mathbf{y}_l|\mathcal{H}_0)} \underset{\mathcal{H}_0}{\overset{\mathcal{H}_1}{\geq}} \delta_L, \quad (16)$$

where δ_L denotes the detection threshold. By taking the logarithm on Δ_L , we have the log-likelihood ratio

$$\log \Delta_L = \sum_{l=1}^L 2\Re(c_{t,l}^* \mathbf{a}_{R,l}^H(\theta_{t,l}) \mathbf{R}_l^{-1} \mathbf{y}_l) - |c_{t,l}|^2 \mathbf{a}_{R,l}^H(\theta_{t,l}) \mathbf{R}_l^{-1} \mathbf{a}_{R,l}(\theta_{t,l}). \quad (17)$$

Maximizing $\log \Delta_L$ with respect to the unknown complex amplitude $c_{t,l}$ by setting $\frac{\partial \log \Delta_L}{\partial c_{t,l}} = 0$ yields

$$\hat{c}_{t,l} = \frac{\mathbf{a}_{R,l}^H(\theta_{t,l}) \mathbf{R}_l^{-1} \mathbf{y}_l}{\mathbf{a}_{R,l}^H(\theta_{t,l}) \mathbf{R}_l^{-1} \mathbf{a}_{R,l}(\theta_{t,l})}. \quad (18)$$

By substituting (18) into (17), the decision statistic of the joint GLRT detector is given as

$$\Gamma = \sum_{l=1}^L \Gamma_l \underset{\mathcal{H}_0}{\overset{\mathcal{H}_1}{\geq}} \gamma_L, \quad (19)$$

where

$$\Gamma_l \triangleq \frac{|\mathbf{a}_{R,l}^H(\theta_{t,l}) \mathbf{R}_l^{-1} \mathbf{y}_l|^2}{\mathbf{a}_{R,l}^H(\theta_{t,l}) \mathbf{R}_l^{-1} \mathbf{a}_{R,l}(\theta_{t,l})} \quad (20)$$

and $\gamma_L = \log \delta_L$ denotes the detection threshold for Γ .

For ease of illustration, we will utilize $\mathbf{a}_{t,l}$ to denote $\mathbf{a}_R(\theta_{t,l})$. Under \mathcal{H}_0 , the signal-under-test only contains clutter and noise. Thus, Γ_l in (20) follows a central chi-square distribution with 2 degrees of freedom (DOF), i.e., $\Gamma_l \sim \chi_2^2(0)$. Under \mathcal{H}_1 , Γ_l follows a chi-square distribution with 2 degrees of freedom (DOF) and non-central parameter μ_l^2 , i.e., $\Gamma_l \sim \chi_2^2(\mu_l^2)$, where $\mu_l^2 = c_{t,l}^2 \mathbf{a}_{t,l}^H \mathbf{R}_l^{-1} \mathbf{a}_{t,l}$. Thus, we have

$$\Gamma = \sum_{l=1}^L \Gamma_l \sim \begin{cases} \chi_{2L}^2(\zeta_L), & \mathcal{H}_1, \\ \chi_{2L}^2(0), & \mathcal{H}_0, \end{cases} \quad (21)$$

where $\zeta_L = \sum_{l=1}^L \mu_l^2$ is the non-central parameter of the chi-square decision statistic Γ .

Following the result in [34], the false alarm probability is given by

$$P_{fa} = e^{-\frac{\gamma_L}{2}} \sum_{l=0}^{L-1} \frac{\left(\frac{\gamma_L}{2}\right)^l}{l!}, \quad (22)$$

indicating that P_{fa} depends on γ_L and L , but is independent of the clutter covariance $\{\mathbf{R}_l\}$. The decision threshold can be determined without prior knowledge of the clutter, i.e., [35]

$$\gamma_L \approx \left(L - \frac{1}{2}\right) + \left(\sqrt{-\frac{8}{5} \ln(4P_{fa}(1 - P_{fa}))} + \sqrt{L - \frac{1}{2}}\right)^2, \quad (23)$$

which is also known as the constant false alarm rate (CFAR) property [25], [33]. Meanwhile, based on (23), the false alarm probability P_{fa} remains a constant as L increases. These properties improve the robustness of the system. Finally, the detection probability can be written as [36]

$$P_d^{(L)} = Q_L\left(\sqrt{\zeta_L}, \sqrt{\gamma_L}\right) = Q_L\left(\sqrt{\sum_{l=1}^L c_{t,l}^2 \mathbf{a}_{t,l}^H \mathbf{R}_l^{-1} \mathbf{a}_{t,l}}, \sqrt{\gamma_L}\right), \quad (24)$$

where $Q_k(\cdot, \cdot)$ denotes the generalized Marcum Q function of order k . In the following, we analyze the impact of the two most important system parameters, namely, the number of antennas at each TMT and the number of TMTs participating in the networked sensing.

B. Array Gain: Impact of multiple antennas in one TMT

In this section, we will investigate the contribution of one TMT through analyzing the non-central parameter μ_l^2 . For that purpose, we first perform the eigen-decomposition on \mathbf{R}_l with

$$\mathbf{R}_l = \mathbf{V}_l \mathbf{\Lambda}_l \mathbf{V}_l^H + \sigma^2 \mathbf{I}, \quad (25)$$

where $\mathbf{V}_l = [\mathbf{v}_{l,1}, \dots, \mathbf{v}_{l,r_l}] \in \mathbb{C}^{N_R \times r_l}$, $\mathbf{\Lambda}_l = \text{Diag}(\lambda_{l,1}, \dots, \lambda_{l,r_l})$ with $r_l \triangleq \text{rank}(\mathbf{A}_{R,l} \mathbf{P}_l \mathbf{A}_{R,l}^H)$.

Therefore, we have

$$\mathbf{R}_l^{-1} = (\mathbf{V}_l \mathbf{\Lambda}_l \mathbf{V}_l^H + \sigma^2 \mathbf{I})^{-1} = \frac{1}{\sigma^2} (\mathbf{I} - \mathbf{V}_l (\sigma_n^2 \mathbf{\Lambda}_l^{-1} + \mathbf{V}_l^H \mathbf{V}_l)^{-1} \mathbf{V}_l^H), \quad (26)$$

where we have used the matrix inversion lemma. In the high clutter to noise ratio (CNR) regime [16], [17], i.e., $\lambda_{l,i} \gg \sigma^2$, we have

$$\mu_l^2 = c_{t,l}^2 \mathbf{a}_{t,l}^H \mathbf{R}_l^{-1} \mathbf{a}_{t,l} \approx \frac{c_{t,l}^2}{\sigma^2} \|\mathbf{P}_{V,l}^\perp \mathbf{a}_{t,l}\|^2 = \text{SNR}_l \cdot \cos^2 \vartheta_{tv,l}^\perp, \quad (27)$$

where $\text{SNR}_l \triangleq \frac{c_{t,l}^2}{\sigma^2}$ denotes the signal-to-noise ratio (SNR) at the l th TMT. Here, $\mathbf{P}_{V,l}^\perp = \mathbf{I} - \mathbf{V}_l (\mathbf{V}_l^H \mathbf{V}_l)^{-1} \mathbf{V}_l^H$ denotes the projector onto the null space of $\text{span}(\mathbf{V}_l)$, and $\vartheta_{tv,l}^\perp$ represents the angle between $\mathbf{P}_{V,l}^\perp \mathbf{a}_{t,l}$ and $\mathbf{a}_{t,l}$. We can rewrite SNR_l as [32]

$$\text{SNR}_l = \frac{C_g N_R P_T}{r_l^\beta}, \quad (28)$$

where C_g is a constant related to the noise variance, reflection coefficient and antenna gains, P_T represents the transmission power, r_l denotes the length of the BS-target-TMT link for the l -th TMT, and β is the path loss exponent. Meanwhile, we have

$$\cos^2(\vartheta_{tv,l}^\perp) = 1 - \cos^2(\vartheta_{tv,l}) = 1 - |\mathbf{a}_{t,l}^H \mathbf{a}_{p,l}|, \quad (29)$$

where $\mathbf{a}_{p,l} \triangleq \mathbf{P}_{V,l} \mathbf{a}_{t,l}$ denotes the orthogonal projection of $\mathbf{a}_{t,l}$ onto $\text{span}(\mathbf{V}_l)$. According to (6), we have $\text{span}(\mathbf{V}_l) = \text{span}(\mathbf{A}_{R,l})$. As a result, there exists a set of positive weights $\{\alpha_{i,l} \in [0, 1]\}$, such that $\mathbf{a}_{p,l} = \sum_{i=1}^P \alpha_{i,l} \mathbf{a}_R(\theta_{l,i})$. It thus follows from (3) that

$$\begin{aligned} |\mathbf{a}_{t,l}^H \mathbf{a}_{p,l}| &= \frac{1}{N_R} \left| \sum_{i=1}^P \sum_{n=1}^{N_R} \alpha_{i,l} e^{j2\pi(n-1)\frac{d}{\lambda}(\cos \theta_{t,l} - \cos \theta_{l,i})} \right| \\ &= \frac{1}{N_R} \left| \sum_{i=1}^P \alpha_{i,l} \frac{e^{j\pi N_R \frac{d}{\lambda}(\cos \theta_{t,l} - \cos \theta_{l,i})} \text{sinc}(\pi N_R \frac{d}{\lambda}(\cos \theta_{t,l} - \cos \theta_{l,i}))}{e^{j\pi \frac{d}{\lambda}(\cos \theta_{t,l} - \cos \theta_{l,i})} \text{sinc}(\pi \frac{d}{\lambda}(\cos \theta_{t,l} - \cos \theta_{l,i}))} \right|, \end{aligned} \quad (30)$$

where we have utilized the Euler's identity, i.e., $2j \sin \theta = e^{j\theta} - e^{-j\theta}$.

Substituting (28) and (30) into (27) yields

$$\mu_l^2 \approx \frac{C_g N_R P_T}{r_l^\beta} \left(1 - \left| \sum_{i=1}^P \alpha_{i,l} e^{j\pi(N_R-1)\frac{d}{\lambda}(\cos \theta_{t,l} - \cos \theta_{l,i})} \frac{\text{sinc}(N_R \Delta_{l,i})}{\text{sinc}(\Delta_{l,i})} \right| \right), \quad (31)$$

where $\text{sinc}(x) = \frac{\sin \pi x}{\pi x}$ and

$$\Delta_{l,i} = \frac{d}{\lambda} (\cos \theta_{t,l} - \cos \theta_{l,i}). \quad (32)$$

Remark 1: It can be observed from (31) that the contribution of the l th TMT is determined by several parameters.

- 1) The length of the BS-Target-TMT link, r_l , affects the SNR exponentially.
- 2) The relation between $\theta_{t,l}$ and $\{\theta_{l,i}\}_{i=1}^P$ affects the ability of the l th TMT to suppress the clutter. To obtain a larger μ_l^2 , we want the summation in (31) to be small. As a result, $\theta_{t,l}$ and $\theta_{l,i}$ are preferred to be far apart, i.e., a TMT with “clearer” view of the target is preferred.
- 3) The number of antennas at the TMT has two effects. On the one hand, SNR_l is directly proportional to N_R , which comes from the antenna array gain. On the other hand, $\cos \vartheta_{tv,l}$ also depends on N_R , which is referred to as the resolution of the TMT. In particular, the mainlobe of $\text{sinc}(N_R\Delta)$ can be obtained by setting $\pi N_R\Delta = \pi$, which gives the boundary of the mainlobe at $\Delta_{ml} = \frac{1}{N_R}$. For the considered ULA, $\text{sinc}(N_R\Delta)$ is approximately 13 dB down from the peak of the mainlobe when Δ is out of $(-\Delta_{ml}/2, \Delta_{ml}/2)$. For given $\theta_{t,l}$ and $\theta_{l,i}$, Δ_{ml} will decrease as N_R increases and the mainlobe of $\text{sinc}(N_R\Delta)$ will become narrower, leading to a larger μ_l^2 .

Remark 2: The impact of multiple antennas in sensing is different from that in communication. For instance, multiple antennas can offer diversity gain in wireless communications. However, for sensing, only the LoS component is utilized and the NLoS components are regarded as part of the clutter. As a result, no diversity gain is provided by multiple receive antennas in sensing applications and Γ_l in (20) only has one complex DOF. However, a larger number of antennas does provide higher array gain and better interference suppression ability, which leads to larger SNR_l and $\cos^2 \vartheta_{tv,l}^\perp$, respectively.

C. Macro-diversity: Contribution of multiple TMTs

In this section, we discuss the benefit of networked sensing.

1) *Impact of the number of TMTs:* It follows from (24) that the detection probability $P_d^{(L)}$ depends on L , ζ_L , and γ_L . The collaboration of multiple TMTs will provide more perspectives for a given target. For instance, when L is larger, it is more likely to find a pair of $\theta_{t,l}$ and $\theta_{l,i}$ which are far apart. However, the detection probability is not a monotonic increasing function of L . Assume there are already L activated TMTs with detection probability $P_d^{(L)}$. Let $P_d^{(L+1)}$ denote the detection probability when a new TMT is selected. In the following, we give a sufficient condition for the contribution of the $(L+1)$ th TMT to be positive.

Algorithm 1: The TMT selection algorithm

- 1) Initialize $n = 0$, $\mathcal{S} = \emptyset$, and $\mathcal{U} = \{1, 2, \dots, M\}$.
 - 2) Find the i_n th TMT from \mathcal{U} that maximizes $\mu_{i_n}^2$, and update $\mathcal{S} = \mathcal{S} \cup \{i_n\}$, $\mathcal{U} = \mathcal{U} \cap \mathcal{S}^c$.
 - 3) $n \leftarrow n + 1$.
 - 4) Repeat 2) to 3) until the conditions in *Proposition 1* is not met.
-

Proposition 1: For a fixed false alarm probability P_{fa} , we have $P_d^{(L+1)} > P_d^{(L)}$, if the following conditions are satisfied:

- 1) The non-central parameter with L TMTs is greater than the detection threshold, i.e., $\zeta_L > \gamma_L$;
- 2) The contribution of the $(L + 1)$ th TMT is greater than the increment of the threshold, i.e.,

$$\mu_{L+1}^2 \geq \gamma_{L+1} - \gamma_L = 2\sqrt{-\frac{8}{5} \ln(4P_{fa}(1 - P_{fa}))} \cdot \left(\sqrt{L + \frac{1}{2}} - \sqrt{L - \frac{1}{2}} \right) + 2. \quad (33)$$

Proof: See Appendix A.

Remark 3: In networked sensing, adding one more TMT will change the distribution of the decision statistics under both hypotheses \mathcal{H}_0 and \mathcal{H}_1 . Thus, for a given false alarm probability, one more TMT will lead to a higher detection threshold, and may not provide a higher detection probability. Consider an extreme case when the link between the target and the $(L + 1)$ th TMT is totally blocked. Under such circumstances, what the new TMT can contribute is only noise, causing a worse probability of detection. *Proposition 1* provides the condition with which the contribution of the $(L + 1)$ th TMT is positive.

2) *TMT Selection Algorithm:* In practice, many TMTs may be around and it is unnecessary and even harmful to activate all TMTs to sense one target. Thus, the selection of TMTs is critical for networked sensing. One application of *Proposition 1* is for TMT selection. Assume there are Q TMTs available in an effective area around the target. We propose a selection algorithm, as summarized in Algorithm 1. In particular, we first calculate μ_l^2 for all available TMTs and order them in descending order. Then, the TMTs are selected based on the condition in *Proposition 1*, i.e., we keep adding new TMTs until the condition no longer holds.

IV. AI-EMPOWERED CLUTTER ESTIMATION

The networked detector needs to know the second order statistics of the clutter, i.e., the covariance matrices $\{\mathbf{R}_l\}_{l=1}^L$. Unfortunately, they are unknown in real application and are normally

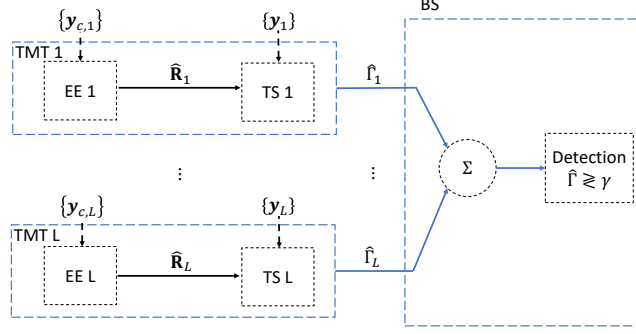


Fig. 3. The diagram of networked sensing.

replaced by their estimates $\{\hat{\mathbf{R}}_l\}_{l=1}^L$. Fig.3 illustrates the diagram of networked sensing, where the covariance matrices $\{\hat{\mathbf{R}}_l\}_{l=1}^L$ are estimated based on the training samples in the CE period, i.e., $\{\mathbf{y}_{c,l}\}$, and utilized for target sensing, based on the received signals of the TMTs in the TS period, i.e., $\{\mathbf{y}_l\}$.

For the networked sensing considered in this paper, there are issues for CE from both communication and computation perspectives. On one hand, estimating $\{\hat{\mathbf{R}}_l\}_{l=1}^L$ for all TMTs by the BS is challenging because moving data from TMTs to the BS can cause very heavy communication burden and lead to serious latency. One possible solution is to estimate $\{\hat{\mathbf{R}}_l\}_{l=1}^L$ at the TMTs to avoid the heavy communication workload. To achieve this, a conventional solution is the widely-used sample covariance matrix (SCM) based method [6]. However, the SCM requires a large number samples to guarantee a considerable performance, which cost high hardware resource and power consumption. However, the TMTs in the PMN are unfortunately power-limited. Moreover, a large number of samples will cause a high hardware consumption and system latency. It is thus necessary to develop some sample-efficient algorithms. Fortunately, the low-rank of the clutter in the mmWave band makes it possible to estimate the covariance matrix by a small amount of data, which can significantly reduce the workload of TMTs. In this section, we propose an efficient and distributed covariance estimation algorithm based on partial data.

A. Clutter Estimation with Partial Data

To reduce the computation workload, the TMTs sample the clutter echo to obtain

$$\mathbf{p}_{c,l}(n) = \mathbf{\Omega}_{l,n} \mathbf{y}_{c,l}(n) \in \mathbb{C}^{p_n \times 1}, n = 1, \dots, N, \quad (34)$$

where $\mathbf{\Omega}_{l,n} \in \mathbb{C}^{p_n \times N_R}$ denotes the sampling matrix at the l th TMT in the n th subframe. In particular, if the (i, j) th entry of $\mathbf{\Omega}_{l,n}$ equals to 1, then the j th entry of $\mathbf{y}_{c,l}(n)$ is selected as the i th entry of $\mathbf{p}_{c,l}(n)$. There is only one “1” in each row of $\mathbf{\Omega}_{l,n}$ and no more than one “1” in each column such that each antenna can only be selected once. Note that the sampling matrix will take p_n values out of the N_R samples. Thus, the sparsity rate is defined as

$$\iota = \frac{1}{NN_R} \sum_{n=1}^N p_n, \quad (35)$$

which represents the volume ratio between the partial data and the complete data. Note that $\mathbf{p}_{c,l}(n) \sim \mathcal{CN}(\mathbf{0}, \mathbf{\Omega}_{l,n} \mathbf{R}_l \mathbf{\Omega}_{l,n}^T)$ because $\mathbf{y}_{c,l}(n) \sim \mathcal{CN}(\mathbf{0}, \mathbf{R}_l)$.

The maximum likelihood (ML) estimate of the covariance matrix based on the partial data can be formulated as

$$\hat{\mathbf{R}}_{\text{ML},l} = \arg \max_{\mathbf{R}_l} \mathcal{L}_{\mathbf{p},l} \left(\mathbf{R}_l \mid \{\mathbf{p}_{c,l}(n)\}_{n=1}^N, \{\mathbf{\Omega}_{l,n}\}_{n=1}^N \right), \quad (36)$$

where

$$\begin{aligned} & \mathcal{L}_{\mathbf{p},l} \left(\mathbf{R}_l \mid \{\mathbf{p}_{c,l}(n)\}_{n=1}^N, \{\mathbf{\Omega}_{l,n}\}_{n=1}^N \right) \\ & \propto - \sum_{n=1}^N p_n \log \pi - \sum_{n=1}^N \left[\log \det (\mathbf{\Omega}_{l,n} \mathbf{R}_l \mathbf{\Omega}_{l,n}^T) + \mathbf{p}_{c,l}^H(n) (\mathbf{\Omega}_{l,n} \mathbf{R}_l \mathbf{\Omega}_{l,n}^T)^{-1} \mathbf{p}_{c,l}(n) \right], \end{aligned} \quad (37)$$

denotes the log-likelihood function of $\hat{\mathbf{R}}_l$ based on $\{\mathbf{p}_{c,l}(n)\}_{n=1}^N$. However, it is difficult to solve (36) directly since a closed-form solution is not available. Moreover, a solution based on an exhausted grid searching in the unknown parameter space could be computationally prohibitive. This motivates us to consider an approximate estimation of \mathbf{R}_l .

B. Expectation-maximization Algorithm

The log-likelihood function of $\hat{\mathbf{R}}_l$ based on the complete data is given as

$$\mathcal{L}_{\mathbf{y},l} \left(\hat{\mathbf{R}}_l \right) = -N \left(N_R \log \pi + \log \det \left(\hat{\mathbf{R}}_l \right) + \text{tr} \left(\hat{\mathbf{R}}_l^{-1} \hat{\mathbf{R}}_{\text{SCM},l} \right) \right), \quad (38)$$

where

$$\hat{\mathbf{R}}_{\text{SCM},l} \triangleq \frac{1}{N} \sum_{n=1}^N \mathbf{y}_{c,l}(n) \mathbf{y}_{c,l}^H(n). \quad (39)$$

However, $\hat{\mathbf{R}}_{\text{SCM},l}$ is not available because the complete data $\{\mathbf{y}_{c,l}(n)\}_{n=1}^N$ is unknown. To solve the above problem, we adopt the EM algorithm, which was proposed to find an approximate ML estimation with incomplete data [37], [38]. The EM algorithm has two steps, i.e., the expectation step (E-step) and the maximization step (M-step).

1) *E-step*: At the E-step of the t th iteration, instead of finding $\mathcal{L}_{y,l}(\widehat{\mathbf{R}}_l)$, we find its conditional expectation

$$\begin{aligned}\bar{\mathcal{L}}(\widehat{\mathbf{R}}_l; \Phi_l^{(t)}) &= \mathbb{E} \left[-N \left(N_R \log \pi + \log \det(\widehat{\mathbf{R}}_l) + \text{tr}(\widehat{\mathbf{R}}_l^{-1} \widehat{\mathbf{R}}_{\text{SCM},l}) \right) \middle| \mathbf{p}_{c,l}(n), \boldsymbol{\Omega}_{l,n}, \widehat{\mathbf{R}}_l^{(t)} \right] \\ &= -N \left(N_R \log \pi + \log \det(\widehat{\mathbf{R}}_l) + \text{tr}(\widehat{\mathbf{R}}_l^{-1} \Phi_l^{(t)}) \right)\end{aligned}\quad (40)$$

where

$$\Phi_l^{(t)} = \frac{1}{N} \sum_{n=1}^N \mathbb{E} \left[\mathbf{y}_{c,l}(n) \mathbf{y}_{c,l}^H(n) \middle| \mathbf{p}_{c,l}(n), \boldsymbol{\Omega}_{l,n}, \widehat{\mathbf{R}}_l^{(t)} \right] = \frac{1}{N} \sum_{n=1}^N \mathbf{S}_n^{(t)}, \quad (41)$$

and

$$\mathbf{S}_n^{(t)} \triangleq \mathbb{E} \left(\mathbf{y}_{c,l}(n) \mathbf{y}_{c,l}^H(n) \middle| \mathbf{p}_{c,l}(n), \boldsymbol{\Omega}_{l,n}, \widehat{\mathbf{R}}_l^{(t)} \right). \quad (42)$$

The following proposition gives the evaluation of $\mathbf{S}_n^{(t)}$.

Proposition 2: The conditional expectation for the covariance matrix of $\mathbf{y}_{c,l}(n)$ is given as

$$\mathbf{S}_n^{(t)} = \left(\boldsymbol{\Omega}_{l,n}^T \mathbf{p}_{c,l}(n) + \bar{\boldsymbol{\Omega}}_{l,n}^T \mathbf{k}_{c,l}^{(t)}(n) \right) \left(\boldsymbol{\Omega}_{l,n}^T \mathbf{p}_{c,l}(n) + \bar{\boldsymbol{\Omega}}_{l,n}^T \mathbf{k}_{c,l}^{(t)}(n) \right)^H + \bar{\boldsymbol{\Omega}}_{l,n}^T \boldsymbol{\Psi}_{l,n}^{(t)} \bar{\boldsymbol{\Omega}}_{l,n}, \quad (43)$$

where

$$\mathbf{k}_{c,l}^{(t)}(n) \triangleq \bar{\boldsymbol{\Omega}}_{l,n} \widehat{\mathbf{R}}_l^{(t)} \boldsymbol{\Omega}_{l,n}^T \left(\boldsymbol{\Omega}_{l,n} \widehat{\mathbf{R}}_l^{(t)} \boldsymbol{\Omega}_{l,n}^T \right)^{-1} \mathbf{p}_{c,l}(n), \quad (44)$$

$$\boldsymbol{\Psi}_{l,n}^{(t)} \triangleq \bar{\boldsymbol{\Omega}}_{l,n} \widehat{\mathbf{R}}_l^{(t)} \bar{\boldsymbol{\Omega}}_{l,n}^T - \bar{\boldsymbol{\Omega}}_{l,n} \widehat{\mathbf{R}}_l^{(t)} \boldsymbol{\Omega}_{l,n}^T \left(\boldsymbol{\Omega}_{l,n} \widehat{\mathbf{R}}_l^{(t)} \boldsymbol{\Omega}_{l,n}^T \right)^{-1} \boldsymbol{\Omega}_{l,n} \widehat{\mathbf{R}}_l^{(t)} \bar{\boldsymbol{\Omega}}_{l,n}^T, \quad (45)$$

and $\bar{\boldsymbol{\Omega}}_{l,n}$ denotes the complement selection of $\boldsymbol{\Omega}_{l,n}$.

Proof: See Appendix B.

By substituting (43) into (40), we can obtain $\bar{\mathcal{L}}(\widehat{\mathbf{R}}_l; \Phi_l^{(t)})$.

2) *M-step*: The M-step finds the update of $\widehat{\mathbf{R}}_l$ that maximizes $\bar{\mathcal{L}}(\widehat{\mathbf{R}}_l; \Phi_l^{(t)})$. The update of $\widehat{\mathbf{R}}_l$ can be obtained by setting

$$\partial \bar{\mathcal{L}}(\widehat{\mathbf{R}}_l; \Phi_l^{(t)}) / \partial \widehat{\mathbf{R}}_l = \widehat{\mathbf{R}}_l^{-1} - \widehat{\mathbf{R}}_l^{-1} \Phi_l^{(t)} \widehat{\mathbf{R}}_l^{-1} = \mathbf{0}, \quad (46)$$

which gives

$$\widehat{\mathbf{R}}_l^{(t+1)} = \Phi_l^{(t)}. \quad (47)$$

However, $\Phi_l^{(t)}$ can be ill-conditioned if the number of samples N is smaller than the dimension N_R . As a result, the inversion operation in (19) may cause serious errors. In the following, we propose an unfolding method to solve this problem.

C. EM-Net: Unfolded EM Algorithm

1) *Penalized EM Estimator*: To tackle the above mentioned ill-conditioned issue, we consider adding a penalty term in $\bar{\mathcal{L}}\left(\widehat{\mathbf{R}}_l; \Phi_l^{(t)}\right)$ to improve the condition number of $\widehat{\mathbf{R}}_l$. It was shown in [39] that the Kullback-Leibler (KL) divergence for Gaussian distributions, i.e.,

$$\mathcal{D}_{\text{KL}}\left(\widehat{\mathbf{R}}_l^{-1}, \mathbf{I}\right) = \text{tr}\left(\widehat{\mathbf{R}}_l^{-1}\right) - \log \det\left(\widehat{\mathbf{R}}_l^{-1}\right) - N_R, \quad (48)$$

can effectively constrain the condition number of $\widehat{\mathbf{R}}_l$. Thus, we adopt the KL divergence penalty and the penalized objective function can be given by

$$\bar{\mathcal{L}}_{\text{pen}}\left(\widehat{\mathbf{R}}_l; \Phi_l^{(t)}\right) = \bar{\mathcal{L}}\left(\widehat{\mathbf{R}}_l; \Phi_l^{(t)}\right) - \alpha_l^{(t)} N \mathcal{D}_{\text{KL}}\left(\widehat{\mathbf{R}}_l^{-1}, \mathbf{I}\right), \quad (49)$$

where $\alpha_l^{(t)}$ denotes the penalty coefficient. The maximizer of (49) gives the update of $\widehat{\mathbf{R}}_l$, i.e.,

$$\widehat{\mathbf{R}}_l^{(t+1)} = (1 - \rho_l^{(t)})\Phi_l^{(t)} + \rho_l^{(t)}\mathbf{I}, \quad (50)$$

where $\rho_l^{(t)} = \frac{\alpha_l^{(t)}}{1 + \alpha_l^{(t)}}$. (50) is a form of shrinkage estimation of the covariance matrix [39], [40], in which $\rho_l^{(t)}$ is referred to as the shrinkage coefficient. The choice of $\rho_l^{(t)}$ has been discussed based on the prior distribution of the original signal in relevant works [39], [40]. However, due to the use of partial data in this paper, the close-form solution of $\rho_l^{(t)}$ is difficult to obtain. In addition, $\rho_l^{(t)}$ changes in each iteration and the number of iterations is unpredictable, which makes the computational complexity of exhausted searching very high. Thus, we consider determining this parameter by the following unfolding method.

2) *EM-Net*: The structure of the EM-Net is illustrated in Fig. 4, which is obtained by unfolding the EM detector and adding several trainable parameters. The network consists of T cascade layers sharing the same architecture but different trainable parameters. The input of the t th layer in the EM-Net is the output from the previous layer. The update in the t -th layer is shown in the lower part of Fig. 4 with the detailed operations as follows

$$\begin{aligned} \Phi_l^{(t)} &= \frac{1}{N} \sum_{n=1}^N \mathbf{S}_n^{(t)}, \\ \Theta_l^{(t+1)} &= (1 - \rho_l^{(t)})\Phi_l^{(t)} + \rho_l^{(t)}\mathbf{I}, \\ \widehat{\mathbf{R}}_l^{(t+1)} &= f_l^{(t)}\left(\Theta_l^{(t+1)}; \xi_l^{(t)}\right), \end{aligned} \quad (51)$$

where the divergence-free estimator $f_l^{(t)}(\cdot)$ is constructed by

$$f_l^{(t)}\left(\Theta_l^{(t+1)}; \xi_l^{(t)}\right) = (1 - \xi_l^{(t)})\Theta_l^{(t+1)} + \xi_l^{(t)}\widehat{\mathbf{R}}_l^{(t)}. \quad (52)$$

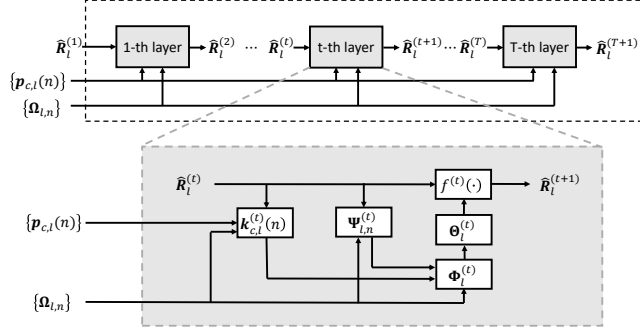


Fig. 4. Diagram of the proposed EM-Net.

With the divergence-free estimator in (52), the estimation results will not change dramatically after the t th layer [41].

Remark 4: The key difference between the EM and EM-Net algorithms is the learnable variables $\mathcal{S}_l = \{\rho_l^{(t)}, \xi_l^{(t)}\}$ in each layer. The learnable parameter $\rho_l^{(t)}$ controls the balance between estimation performance and the condition number. Another learnable parameter $\xi_l^{(t)}$ in the linear estimator $f_l^{(t)}(\cdot)$ plays an important role in constructing an appropriate divergence-free estimator. The original EM estimator in (47) can be interpreted as a special case of EM-net by setting $\rho_l^{(t)} = 0$ and $\xi_l^{(t)} = 0$. By optimizing the learnable parameters in the training process, the estimation performance can be improved.

Remark 5: Here, we assess the computational complexity of the proposed EM and EM-Net algorithms for one TMT. The complexity is dominated by the order of the number of complex-valued multiply operations. Recalling (42), the complexity of SCM is $\mathcal{O}(NN_R^2)$. However, to achieve a considerable performance, a large number of samples are required, which leads to high hardware and power consumption. Moreover, SCM is not suitable for the sparsely sampled data. The complexity of the EM-Net is similar to that of the EM because the EM-Net has a similar structure to the EM, but with some learnable parameters. Recalling (47) and (48), the complexity of obtaining $\mathbf{k}_{c,l}^{(t)}(n)$ and $\Psi_{l,n}^{(t)}$ are dominated by the inverse of a $p_n \times p_n$ matrix, whose computational complexity is about $\mathcal{O}(p_n^3)$. The computational complexity of (44) is about $\mathcal{O}(NN_R^2 + \sum_{n=1}^N p_n^3)$. Given the EM-Net has T layers, the overall computational complexity is $\mathcal{O}(TNN_R^2 + \sum_{n=1}^N Tp_n^3)$. In general, the computational complexity of the EM-Net is higher than that of SCM with the same number of samples. However, as shown in the

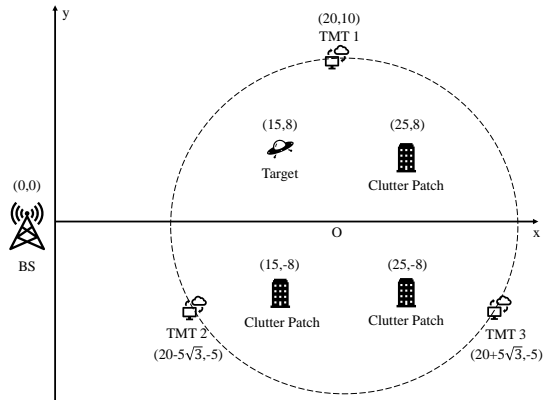


Fig. 5. The illustration of simulation scenario.

simulation part, the EM-Net algorithm can significantly reduce the requirement of samples. It indicates that the EM-Net can reduce the hardware and power consumption and system latency, which is attractive to real applications.

V. SIMULATION

In this section, we show the performance of the proposed networked sensing. Consider a PMN where the BSs are equipped with $N_T = 32$ antennas. The carrier frequency is set to 28 GHz and $\beta = 2$ [32]. The noise power σ^2 is set as -90 dBm. We set $\frac{1}{L} \sum_{i=1}^P \sum_{l=1}^L \sigma_{l,i}^2 / \sigma^2 = 30$ dB unless otherwise specified. The channel between the BS and the k th UE is modeled as shown in (4), where $\epsilon_{l,i}(n) \sim \mathcal{CN}(0, 10^{-0.1(\kappa+\mu)})$ denotes the complex gain of the i -th path in the n -th subframe. Here, κ is the path loss defined as $\kappa = a + 10b \log_{10}(d) + \epsilon$ with d denoting the distance between the BS and the k th UE and $\epsilon \sim \mathcal{CN}(0, \sigma_\epsilon^2)$ [42]. Following [42], we set $a = 61.4$, $b = 2$, and $\sigma_\epsilon = 5.8$ dB. The channel is assumed to follow Rician fading, where the Rician factor is set as 7 dB for the LoS component and 0 dB for the NLoS component. For a given false alarm probability P_{fa} , the detection threshold γ_L is obtained by (23). Then, 100000 Monte-Carlo trails are performed to obtain P_d .

A. Detection Performance

Consider a PMN with one BS and 3 TMTs, as illustrated in Fig. 5. Assume that there are one target and 3 clutter patches in the environment. The coordinates of the BS, the target, the clutter patches and the TMTs are respectively given as $(0, 0)$, $(15, 8)$, $\{(25, 8), (15, -8), (25, -8)\}$, and

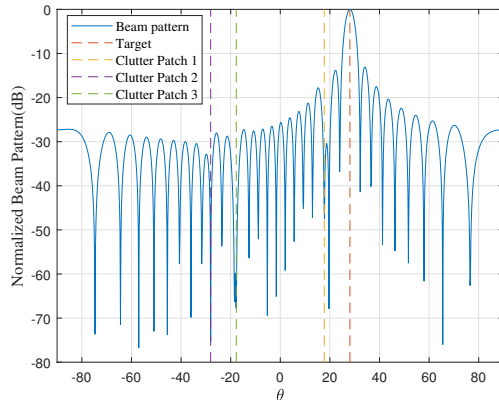


Fig. 6. The normalized transmitting beam pattern.

$\{(20, 10), (20 - 5\sqrt{3}, -5), (20 + 5\sqrt{3}, -5)\}$ where all coordinates are in meters. The AOD and AOA of the ST, UEs and clutter patches are determined based on the geometric locations. For each abscissa, 5000 Monte-Carlo trials are performed.

We first show the beam pattern which is given by

$$P(\theta) = |\mathbf{f}_\perp \mathbf{a}_T(\theta)|^2, \theta \in \Theta, \quad (53)$$

where $\Theta = [-\frac{\pi}{2}, \frac{\pi}{2}]$. The beam pattern measures the transmitted power at the direction θ . For clarity, the beam pattern is normalized by

$$P_N(\theta) = \frac{P(\theta)}{\max_{\theta \in \Theta} P(\theta)}.$$

From Fig. 6, we can see that the power transmitted to the clutter patches is lower than -40 dB. That is, the sensing precoder will not significantly affect the clutter patches.

Fig. 7 shows the accuracy of the theoretical results regarding the detection threshold and the detection probability, respectively. The legend ‘‘Simulated Results’’ indicates the results obtained by Monte-Carlo trials, while ‘‘Theoretical Results’’ represents the detection threshold and the detection probability obtained by (23) and (24), respectively. It can be observed that the theoretical results match the simulation results very well.

B. Array Gain

It follows from (27) that the number of antennas N_R influences μ_l^2 through SNR_l and $\cos^2 \theta_{tv,l}^\perp$. Parts (a) and (b) of Fig. 8 show the impact of N_R on SNR_l and $\cos^2 \theta_{tv,l}^\perp$, respectively, where

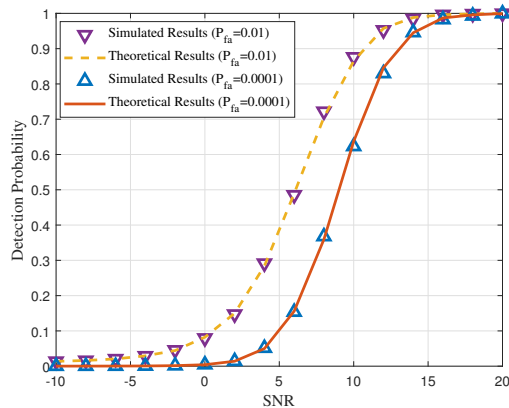


Fig. 7. Accuracy of Performance Analysis for Detection Probability $P_d^{(L)}$.

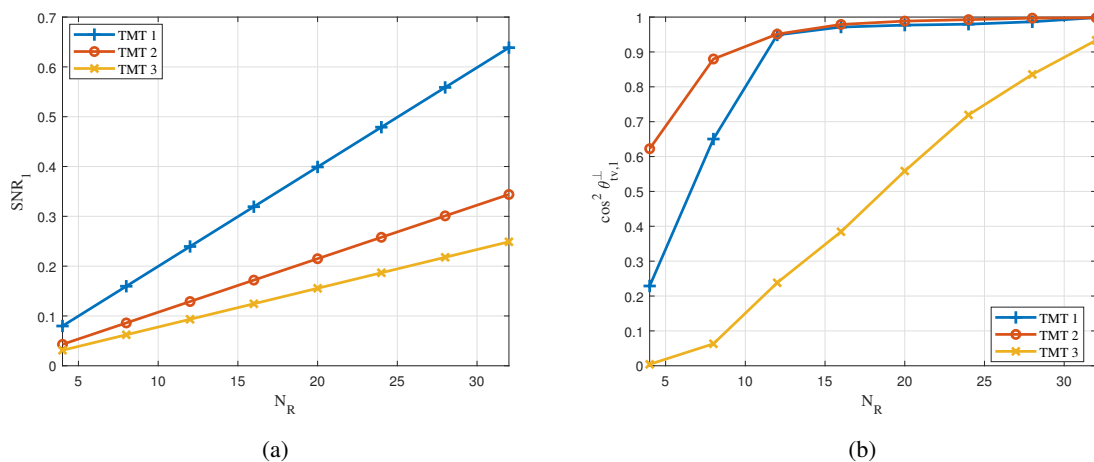


Fig. 8. Effect of the number of antennas N_R . (a) SNR_l (b) $\cos^2 \theta_{tv,l}^\perp$.

we set $C_g = 10$ and $P_T = 1$, and the other settings are the same as Fig. 7. It can be observed that SNR_l grows linearly with N_R due to the array gain. However, the improvement of $\cos^2 \theta_{tv,l}^\perp$ depends on the relative locations of the target and the clutter patches as shown in Fig. 5. For example, $\cos^2 \theta_{tv,2}^\perp$ for TMT-2 increases quickly due to the clear link. However, $\cos^2 \theta_{tv,3}^\perp$ for TMT-3 grows very slowly due to the two nearby clutter patches.

C. Macro-Diversity

Next, we show the effect of the number of TMTs. For that purpose, we assume there are in total Q TMTs available and show the performance when L of them are selected. We set $C_g = 10$ and $P_T = 0.5$, and the locations of the clutter patches are the same as those in Fig. 5. The Q

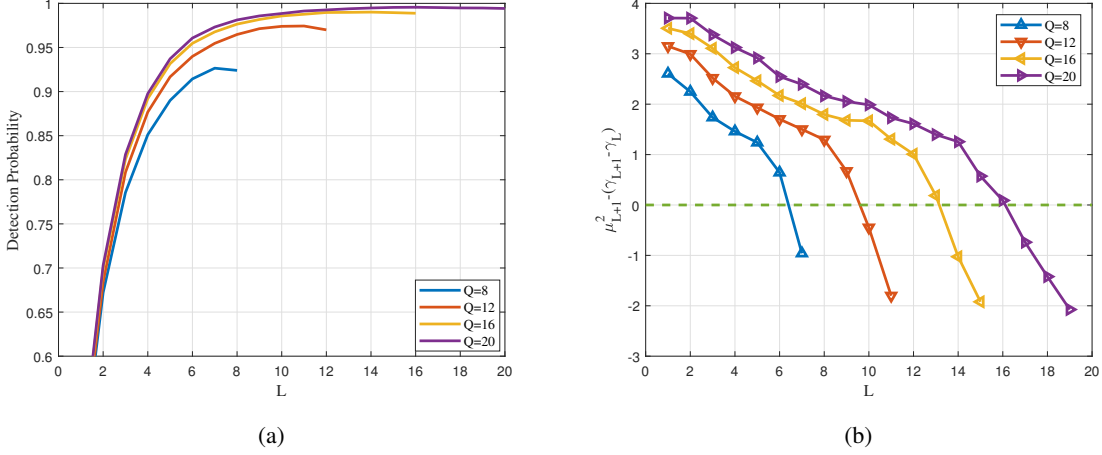


Fig. 9. Detection Probability versus the number of selected TMTs L and the number of deployed TMTs Q . (a) The effect of L with fixed Q ; (b) The difference between the increment of ζ_L and γ_L : $\mu_{L+1}^2 - (\gamma_{L+1} - \gamma_L)$.

TMTs are evenly located on a circle \mathcal{O} with a radius of 10m, where the coordinates of the i th TMT are given as $\left[20 + 10 \sin(2\pi \frac{i-1}{Q}), 10 \cos(2\pi \frac{i-1}{Q})\right]$, $i = 1, 2, \dots, Q$. The target is randomly generated within the circle \mathcal{O} . For each abscissa, 10000 Monte-Carlo trials are performed and we set $P_{fa} = 0.01$.

Fig. 9 shows the detection probability P_d when the best L out of Q TMTs are selected. In particular, we calculate $\{\mu_i^2\}_{i=1}^Q$ for all TMTs and arrange them in the descending order, i.e., $\mu_{i(1)}^2 \geq \mu_{i(2)}^2 \geq \dots \mu_{i(Q)}^2$. Then the L TMTs with the highest μ_i^2 are selected. We have several observations. First, for a given L , P_d is a non-decreasing function of Q due to the selection diversity. However, for a given Q , P_d is not a monotonic increasing function of L . In fact, P_d will first increase, then stabilize, and finally decrease. This agrees with the discussion in Remark 3.

Next, we illustrate the performance of the proposed TMT selection algorithm. Assume L TMTs have been selected. Fig. 9b shows the difference between the increment of ζ_L and γ_L , i.e., $\mu_{L+1}^2 - (\gamma_{L+1} - \gamma_L)$. According to *Proposition 1*, adding the new TMT will benefit P_d , if $\mu_{L+1}^2 \geq \gamma_{L+1} - \gamma_L$. We can observe from Fig. 9b that $\mu_{L+1}^2 - (\gamma_{L+1} - \gamma_L)$ is positive when L is small, but as L increases, $\mu_{L+1}^2 - (\gamma_{L+1} - \gamma_L)$ decreases and then becomes negative. For example, when $Q = 12$, the cross-zero point is between $L = 9$ and $L = 10$, i.e., $\mu_{11}^2 < (\gamma_{11} - \gamma_{10})$. Therefore, Algorithm 1 will stop at $L = 10$. But, the optimal P_d is achieved at $L = 11$ as shown in Fig. 9a. This is because the conditions in *Proposition 1* are sufficient but not necessary. As

a result, the proposed algorithm gives a conservative but relatively accurate estimation for the optimal number of TMT. Such a conservative estimation is preferred from the system complexity point of view.

D. Covariance Matrix Estimation

Next, we show the performance of the proposed EM-Net algorithm for CE. Unless otherwise specified, the number of the antennas at one TMT and the number of communication subframes in the CE period are set as $N_R = 16$ and $N = 50$, respectively. We set the number of TMTs and clutter patches to be $L = 3$ and $P = 3$. The coordinates of the TMTs and clutter patches are the same as those in Sec. V.A, and the target is randomly generated in the circle \mathcal{O} . Here, we set $P_{fa} = 0.01$.

For the training process, the learnable parameters are optimized by the stochastic gradient descent method. In our experiments, the loss function used for training is selected as

$$f_{loss} = \left(\frac{1}{N_{\text{layer}}} \sum_{i=1}^{N_{\text{layer}}} \text{SL} \left(\mathbf{R}^{(i)}, \widehat{\mathbf{R}}^{(i)}, \mathbf{a}_t \right) \right)^{-1} \quad (54)$$

where N_{layer} denotes the number of layers in the training process, and

$$\text{SL} \left(\mathbf{R}, \widehat{\mathbf{R}}, \mathbf{a}_t \right) = \frac{\left(\mathbf{a}_t^H \widehat{\mathbf{R}}^{-1} \mathbf{a}_t \right)^2}{\left(\mathbf{a}_t^H \mathbf{R}^{-1} \mathbf{a}_t \right) \left(\mathbf{a}_t^H \widehat{\mathbf{R}}^{-1} \mathbf{R} \widehat{\mathbf{R}}^{-1} \mathbf{a}_t \right)} \quad (55)$$

denotes the SCNR loss of the covariance estimation, i.e., the ratio between the SCNR with the estimated covariance matrix and that with the real covariance matrix, which is widely used to measure the performance of covariance estimation in radar detection [16], [17], [25], [39]. The smaller the SCNR loss is, the better the detection performance will be. The number of layers is set as $N_{\text{layer}} = 10$. The number of batches for training process is set as $N_{\text{batch}} = 1500$. The batch size for each iteration is set as the total number of the communication subframes. We compare the performance of the EM and EM-Net estimators with the classical SCM estimator which utilizes the complete data.

1) *Convergence Performance*: First, we illustrate the convergence of the EM and EM-Net estimators. It can be observed from Fig. 10 that the EM and EM-Net detectors converge within 10 and 5 layers (iterations), respectively. Meanwhile, the EM-Net detector can achieve a lower training loss.

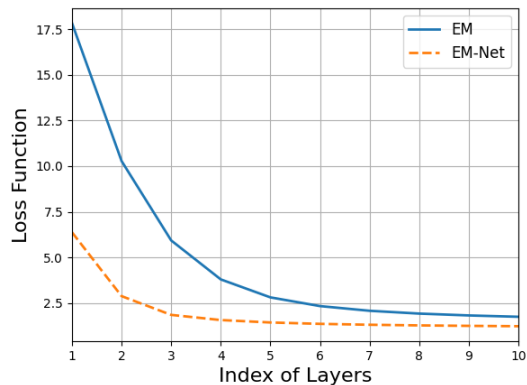


Fig. 10. Loss function of the proposed EM and EM-Net estimators versus the number of layers.

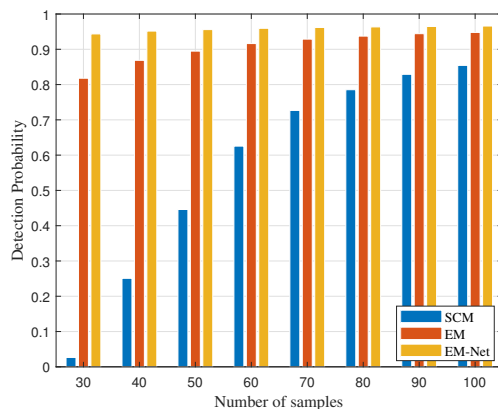


Fig. 11. Detection probability versus the sample sizes for clutter estimation.

2) *Effect of Sample Size for Clutter Estimation:* Fig. 11 shows the detection probability versus the sample size for clutter estimation. We set $N_R = 16$, SNR = 10 dB, and $\iota = 0.5$ for all TMTs, while SCM requires the complete data. For each abscissa, 2000 Monte-Carlo trials are performed. It can be observed that the detection performance will improve as the sample size increases. Furthermore, EM-Net outperforms EM which can achieve a better detection performance than SCM, and the performance gap is larger with less samples.

3) *Effect of the Sparsity Rate:* Fig. 12 depicts the detection probability versus SNR under different sparsity rates. The legend ‘‘Optimal’’ indicates the detection performance with the real covariance matrix. For each abscissa, 2000 Monte-Carlo trials are performed. From Fig. 12, we can observe that EM-Net outperforms EM for different sparsity rates, indicating that the

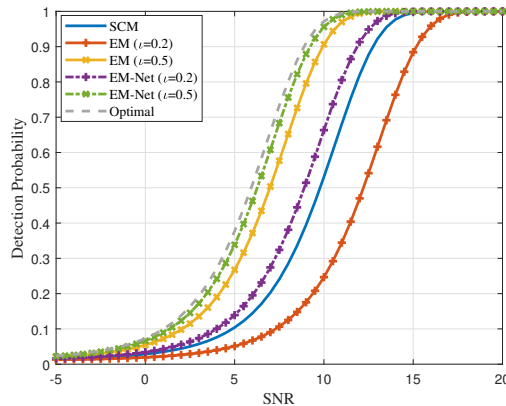


Fig. 12. Detection Probability under different sparsity rate.

introduced learnable parameters improve the estimation performance. Meanwhile, the detection performance of SCM is between EM and EM-Net with $\iota = 0.2$, which shows that the proposed EM-Net can achieve better estimation performance with less data samples.

VI. CONCLUSION

This paper investigated networked sensing in PMNs with the presence of clutter. A networked detector was developed to exploit the macro-diversity from multiple TMTs and the array gain from multiple receive antennas. Performance analysis illustrated the impact of the macro-diversity and array gain on networked sensing. It was shown that, although multiple TMTs provide macro-diversity, the detection probability is not a monotonic increasing function of the number of activated TMTs. A sufficient condition for one more TMT's contribution to be positive was derived, with which a TMT selection algorithm was proposed. On the other hand, although multiple receive antennas bring array gain, they no longer provide diversity gain for sensing because only the LoS component is used, which is different from communication. To improve the efficiency of clutter estimation, an unfolded EM algorithm was proposed where only the partial data are required for estimating the clutter covariance. Networked sensing brings unprecedented opportunities to exploit the well-developed infrastructure of cellular networks for sensing purposes, but at the same time faces serious challenges in terms of communication and computation efficiency, due to the collaboration between distributed nodes. This work revealed the advantage of networked sensing together with the impact of several key network parameters, and demonstrated the high efficiency of machine learning empowered clutter estimation algorithms.

APPENDIX A

PROOF OF PROPOSITION 1

Before the proof, we define an auxiliary function $\mathcal{F}_v(a, b) = \frac{\mathcal{Q}_{v+1}(\sqrt{a}, \sqrt{b})}{\mathcal{Q}_v(\sqrt{a}, \sqrt{b})}$ and introduce some important theorems as follows.

Theorem 1 (Monotonicity, [43, Theorem 1]): The generalized Marcum Q-function $\mathcal{Q}_v(a, b)$ is strictly increasing in v and a for all $a \geq 0$ and $b, v > 0$, and is strictly decreasing in b for all $a, b \geq 0$ and $v > 0$.

Theorem 2: The derivative of $\log \mathcal{Q}_v(\sqrt{a}, \sqrt{b})$ with respect to a and b are respectively obtained as

$$\frac{\partial \log \mathcal{Q}_v(\sqrt{a}, \sqrt{b})}{\partial a} = \frac{1}{2} \cdot \frac{\mathcal{Q}_{v+1}(\sqrt{a}, \sqrt{b})}{\mathcal{Q}_v(\sqrt{a}, \sqrt{b})} - \frac{1}{2}, \quad (56a)$$

$$\frac{\partial \log \mathcal{Q}_v(\sqrt{a}, \sqrt{b})}{\partial b} = \frac{1}{2} \cdot \frac{\mathcal{Q}_{v-1}(\sqrt{a}, \sqrt{b})}{\mathcal{Q}_v(\sqrt{a}, \sqrt{b})} - \frac{1}{2}. \quad (56b)$$

Proof: (56a) and (56b) can be directly derived by the chain rule as follows:

$$\begin{aligned} \frac{\partial \log \mathcal{Q}_v(\sqrt{a}, \sqrt{b})}{\partial a} &= \frac{\partial \log \mathcal{Q}_v(\sqrt{a}, \sqrt{b})}{\partial \mathcal{Q}_v(\sqrt{a}, \sqrt{b})} \cdot \frac{\partial \mathcal{Q}_v(\sqrt{a}, \sqrt{b})}{\partial \sqrt{a}} \cdot \frac{\partial \sqrt{a}}{\partial a} \\ &= \frac{1}{\mathcal{Q}_v(\sqrt{a}, \sqrt{b})} \cdot \left[\sqrt{a} \left(\mathcal{Q}_{v+1}(\sqrt{a}, \sqrt{b}) - \mathcal{Q}_v(\sqrt{a}, \sqrt{b}) \right) \right] \cdot \frac{1}{2\sqrt{a}} \\ &= \frac{1}{2} \cdot \frac{\mathcal{Q}_{v+1}(\sqrt{a}, \sqrt{b})}{\mathcal{Q}_v(\sqrt{a}, \sqrt{b})} - \frac{1}{2}. \end{aligned} \quad (57)$$

$$\begin{aligned} \frac{\partial \log \mathcal{Q}_v(\sqrt{a}, \sqrt{b})}{\partial b} &= \frac{\partial \log \mathcal{Q}_v(\sqrt{a}, \sqrt{b})}{\partial \mathcal{Q}_v(\sqrt{a}, \sqrt{b})} \cdot \frac{\partial \mathcal{Q}_v(\sqrt{a}, \sqrt{b})}{\partial \sqrt{b}} \cdot \frac{\partial \sqrt{b}}{\partial b} \\ &= \frac{1}{\mathcal{Q}_v(\sqrt{a}, \sqrt{b})} \cdot \left[\sqrt{b} \left(\mathcal{Q}_{v-1}(\sqrt{a}, \sqrt{b}) - \mathcal{Q}_v(\sqrt{a}, \sqrt{b}) \right) \right] \cdot \frac{1}{2\sqrt{b}} \\ &= \frac{1}{2} \cdot \frac{\mathcal{Q}_{v-1}(\sqrt{a}, \sqrt{b})}{\mathcal{Q}_v(\sqrt{a}, \sqrt{b})} - \frac{1}{2}. \end{aligned} \quad (58)$$

■

Theorem 3: The auxiliary function $b \mapsto \mathcal{F}_v(a, b)$ is monotonically decreasing for $a \geq b > 0$.

Proof: For all $a \geq 0$ and $b, v > 0$, since $\mathcal{Q}_v(a, b)$ is strictly increasing in v [43, Theorem 1], we have $\mathcal{Q}_v(\sqrt{a}, \sqrt{b}) < \mathcal{Q}_{v+1}(\sqrt{a}, \sqrt{b})$. Meanwhile, in view of [44, Theorem 3.1(b)], the function $v \mapsto \mathcal{Q}_{v+1}(\sqrt{a}, \sqrt{b}) - \mathcal{Q}_v(\sqrt{a}, \sqrt{b})$ is strictly decreasing on $(0, +\infty)$ for $a \geq b > 0$. Thus, we have $\mathcal{Q}_{v+1}(\sqrt{a}, \sqrt{b}) - \mathcal{Q}_v(\sqrt{a}, \sqrt{b}) < \mathcal{Q}_v(\sqrt{a}, \sqrt{b}) - \mathcal{Q}_{v-1}(\sqrt{a}, \sqrt{b})$. We know that

$\frac{x}{y} > \frac{x+u}{y+v}$ for all $0 < y < x$ and $0 < u < v$. Thus, invoking $x = \mathcal{Q}_v(\sqrt{a}, \sqrt{b})$, $y = \mathcal{Q}_{v-1}(\sqrt{a}, \sqrt{b})$, $u = \mathcal{Q}_{v+1}(\sqrt{a}, \sqrt{b}) - \mathcal{Q}_v(\sqrt{a}, \sqrt{b})$, and $v = \mathcal{Q}_v(\sqrt{a}, \sqrt{b}) - \mathcal{Q}_{v-1}(\sqrt{a}, \sqrt{b})$, we have

$$\mathcal{F}_v(a, b) = \frac{\mathcal{Q}_v(\sqrt{a}, \sqrt{b}) + \left(\mathcal{Q}_{v+1}(\sqrt{a}, \sqrt{b}) - \mathcal{Q}_v(\sqrt{a}, \sqrt{b}) \right)}{\mathcal{Q}_{v-1}(\sqrt{a}, \sqrt{b}) + \left(\mathcal{Q}_v(\sqrt{a}, \sqrt{b}) - \mathcal{Q}_{v-1}(\sqrt{a}, \sqrt{b}) \right)} < \mathcal{F}_{v-1}(a, b). \quad (59)$$

Theorem 4: For all $a, b \geq 0$, $\Delta a, \Delta b > 0$, and $v > 0$, we have

$$\log \mathcal{Q}_v(\sqrt{a + \Delta a}, \sqrt{b}) - \log \mathcal{Q}_v(\sqrt{a}, \sqrt{b}) \geq \left(\frac{1}{2} \cdot \frac{\mathcal{Q}_{v+1}(\sqrt{a + \Delta a}, \sqrt{b})}{\mathcal{Q}_v(\sqrt{a + \Delta a}, \sqrt{b})} - \frac{1}{2} \right) \Delta a, \quad (60a)$$

$$\log \mathcal{Q}_v(\sqrt{a}, \sqrt{b + \Delta b}) - \log \mathcal{Q}_v(\sqrt{a}, \sqrt{b}) \geq \left(\frac{1}{2} \cdot \frac{\mathcal{Q}_{v-1}(\sqrt{a}, \sqrt{b + \Delta b})}{\mathcal{Q}_v(\sqrt{a}, \sqrt{b + \Delta b})} - \frac{1}{2} \right) \Delta b. \quad (60b)$$

Proof: Since $a \mapsto \mathcal{Q}_v(\sqrt{a}, \sqrt{b})$ and $b \mapsto \mathcal{Q}_v(\sqrt{a}, \sqrt{b})$ are both log-concave for all $a, b \leq 0$ and $v > 0$ [43], [44], the function $a \mapsto \log \mathcal{Q}_v(\sqrt{a}, \sqrt{b})$ and $b \mapsto \log \mathcal{Q}_v(\sqrt{a}, \sqrt{b})$ are both concave.

We begin with proving (60a). According to the mean value theorem [45], there exists a point ξ in $(a, a + \Delta a)$ such that

$$\log \mathcal{Q}_v(\sqrt{a + \Delta a}, \sqrt{b}) - \log \mathcal{Q}_v(\sqrt{a}, \sqrt{b}) = \left. \frac{\partial \log \mathcal{Q}_v(\sqrt{a}, \sqrt{b})}{\partial a} \right|_{a=\xi} \cdot \Delta a. \quad (61)$$

Given the property of the concave function, we have

$$\left. \frac{\partial \log \mathcal{Q}_v(\sqrt{a}, \sqrt{b})}{\partial a} \right|_{a=\xi} \geq \left. \frac{\partial \log \mathcal{Q}_v(\sqrt{a}, \sqrt{b})}{\partial a} \right|_{a=a+\Delta a}. \quad (62)$$

In view of (61) and (62), the inequality in (60a) is proved based on *Theorem 2*. Similarly, the inequality in (60b) can be obtained. \blacksquare

Next, we will prove *Proposition 1*. Given $P_d^{(L+1)} > 0$ and $P_d^{(L)} > 0$, we have

$$\log \frac{P_d^{(L+1)}}{P_d^{(L)}} = \log \mathcal{Q}_{L+1}(\sqrt{\zeta_{L+1}}, \sqrt{\gamma_{L+1}}) - \log \mathcal{Q}_L(\sqrt{\zeta_L}, \sqrt{\gamma_L}) = \mathcal{A}_1 + \mathcal{A}_2 + \mathcal{A}_3, \quad (63)$$

where

$$\begin{aligned} \mathcal{A}_1 &= \log \mathcal{Q}_{L+1}(\sqrt{\zeta_{L+1}}, \sqrt{\gamma_{L+1}}) - \log \mathcal{Q}_{L+1}(\sqrt{\zeta_{L+1}}, \sqrt{\gamma_L}), \\ \mathcal{A}_2 &= \log \mathcal{Q}_{L+1}(\sqrt{\zeta_{L+1}}, \sqrt{\gamma_L}) - \log \mathcal{Q}_L(\sqrt{\zeta_{L+1}}, \sqrt{\gamma_L}), \\ \mathcal{A}_3 &= \log \mathcal{Q}_L(\sqrt{\zeta_{L+1}}, \sqrt{\gamma_L}) - \log \mathcal{Q}_L(\sqrt{\zeta_L}, \sqrt{\gamma_L}). \end{aligned} \quad (64)$$

Recalling (21), \mathcal{A}_1 , \mathcal{A}_2 , and \mathcal{A}_3 represent the increment of detection probability with respect to the detection threshold γ_L , the degree of the decision statistic L , and the non-central parameter ζ_L , respectively. By observing *Theorem 1*, we have that $\mathcal{A}_2 \geq 0$, $\mathcal{A}_3 \geq 0$, and $\mathcal{A}_1 < 0$. The

first two inequalities hold because increasing the DOF and the non-central parameter of Γ_L will increase the detection probability. However, a larger γ_L will decrease $P_d^{(L)}$, which leads to $\mathcal{A}_1 < 0$.

By applying *Theorem 4*, we have

$$\begin{aligned} \mathcal{A}_1 &\geq \left(\frac{1}{2} \cdot \frac{\mathcal{Q}_L(\sqrt{\zeta_{L+1}}, \sqrt{\gamma_{L+1}})}{\mathcal{Q}_{L+1}(\sqrt{\zeta_{L+1}}, \sqrt{\gamma_{L+1}})} - \frac{1}{2} \right) (\gamma_{L+1} - \gamma_L) \\ &= -\frac{1}{2} \left(1 - \frac{1}{\mathcal{F}_L(\zeta_{L+1}, \gamma_{L+1})} \right) (\gamma_{L+1} - \gamma_L), \end{aligned} \quad (65)$$

$$\mathcal{A}_3 \geq \left(\frac{1}{2} \cdot \frac{\mathcal{Q}_{L+1}(\sqrt{\zeta_{L+1}}, \sqrt{\gamma_L})}{\mathcal{Q}_L(\sqrt{\zeta_{L+1}}, \sqrt{\gamma_L})} - \frac{1}{2} \right) \mu_{L+1}^2 = \frac{1}{2} (\mathcal{F}_L(\zeta_{L+1}, \gamma_L) - 1) \mu_{L+1}^2. \quad (66)$$

Recalling the conditions 1) and 2) in *Proposition 1*, we have $\zeta_{L+1} > \gamma_{L+1} > 0$ and $\zeta_{L+1} > \gamma_L > 0$, which means that *Theorem 3* holds true for both $\mathcal{F}_L(\zeta_{L+1}, \gamma_{L+1})$ and $\mathcal{F}_L(\zeta_{L+1}, \gamma_L)$. Applying *Theorem 3* yields $\mathcal{F}_L(\zeta_{L+1}, \gamma_{L+1}) < \mathcal{F}_L(\zeta_{L+1}, \gamma_L)$. Thus, we have

$$\mathcal{F}_L(\zeta_{L+1}, \gamma_L) \mathcal{F}_L(\zeta_{L+1}, \gamma_{L+1}) - 2\mathcal{F}_L(\zeta_{L+1}, \gamma_{L+1}) + 1 \geq (\mathcal{F}_L(\zeta_{L+1}, \gamma_{L+1}) - 1)^2 \geq 0, \quad (67)$$

By rearranging (67), we have

$$1 - \frac{1}{\mathcal{F}_L(\zeta_{L+1}, \gamma_{L+1})} \leq \mathcal{F}_L(\zeta_{L+1}, \gamma_L) - 1. \quad (68)$$

From *Theorem 1*, we have $\mathcal{F}_v(a, b) > 1$, such that $1 - \frac{1}{\mathcal{F}_L(\zeta_{L+1}, \gamma_{L+1})} > 0$ and $\mathcal{F}_L(\zeta_{L+1}, \gamma_L) - 1 > 0$.

Based on (33) and (68), we can rewrite (66) as

$$\mathcal{A}_3 \geq \frac{1}{2} \left(1 - \frac{1}{\mathcal{F}_L(\zeta_{L+1}, \gamma_{L+1})} \right) (\gamma_{L+1} - \gamma_L) = -\mathcal{A}_1, \quad (69)$$

which gives $\mathcal{A}_1 + \mathcal{A}_3 \geq 0$. Given $\mathcal{A}_2 \geq 0$, we have

$$\log \frac{P_d^{(L+1)}}{P_d^{(L)}} = \mathcal{A}_1 + \mathcal{A}_2 + \mathcal{A}_3 \geq 0. \quad (70)$$

It follows that $P_d^{(L+1)} > P_d^{(L)}$, which completes the proof. \blacksquare

APPENDIX B

PROOF OF PROPOSITION 2

First, we define $\mathbf{Q}_{l,n} = [\boldsymbol{\Omega}_{l,n}^\top, \bar{\boldsymbol{\Omega}}_{l,n}^\top]^\top$, and it can be validated that $\mathbf{Q}_{l,n}^\top \mathbf{Q}_{l,n} = \mathbf{I}$. Then, we have

$$\mathbf{S}_n^{(t)} = \mathbb{E} \left(\mathbf{y}_{c,l}(n) \mathbf{y}_{c,l}^H(n) \mid \mathbf{p}_{c,l}(n), \boldsymbol{\Omega}_{l,n}, \hat{\mathbf{R}}_l^{(t)} \right) = \mathbf{Q}_{l,n}^\top \boldsymbol{\Xi}_n \mathbf{Q}_{l,n}, \quad (71)$$

where

$$\begin{aligned} \Xi_n &\triangleq \mathbb{E} \left(\mathbf{Q}_{l,n} \mathbf{y}_{c,l}(n) \mathbf{y}_{c,l}^H(n) \mathbf{Q}_{l,n}^T \mid \mathbf{p}_{c,l}(n), \boldsymbol{\Omega}_{l,n}, \widehat{\mathbf{R}}_l^{(t)} \right) \\ &= \begin{bmatrix} \mathbf{p}_{c,l} \mathbf{p}_{c,l}^H & \mathbf{p}_{c,l} \mathbb{E} \left(\mathbf{y}_{c,l}^H(n) \overline{\boldsymbol{\Omega}}_{l,n}^T \mid \mathbf{p}_{c,l}(n), \boldsymbol{\Omega}_{l,n}, \widehat{\mathbf{R}}_l^{(t)} \right) \\ \mathbb{E} \left(\overline{\boldsymbol{\Omega}}_{l,n} \mathbf{y}_{c,l}(n) \mid \mathbf{p}_{c,l}(n), \boldsymbol{\Omega}_{l,n}, \widehat{\mathbf{R}}_l^{(t)} \right) \mathbf{p}_{c,l}^H & \mathbb{E} \left(\overline{\boldsymbol{\Omega}}_{l,n} \mathbf{y}_{c,l}(n) \mathbf{y}_{c,l}^H(n) \overline{\boldsymbol{\Omega}}_{l,n}^T \mid \mathbf{p}_{c,l}(n), \boldsymbol{\Omega}_{l,n}, \widehat{\mathbf{R}}_l^{(t)} \right) \end{bmatrix}. \end{aligned} \quad (72)$$

Given $\overline{\boldsymbol{\Omega}}_{l,n} \mathbf{y}_{c,l}(n)$ follows the Gaussian distribution, we have [46]

$$\mathbb{E} \left(\overline{\boldsymbol{\Omega}}_{l,n} \mathbf{y}_{c,l}(n) \mid \mathbf{p}_{c,l}(n), \boldsymbol{\Omega}_{l,n}, \widehat{\mathbf{R}}_l^{(t)} \right) = \mathbf{k}_{c,l}^{(t)}(n), \quad (73)$$

$$\mathbb{E} \left(\overline{\boldsymbol{\Omega}}_{l,n} \mathbf{y}_{c,l}(n) \mathbf{y}_{c,l}^H(n) \overline{\boldsymbol{\Omega}}_{l,n}^T \mid \mathbf{p}_{c,l}(n), \boldsymbol{\Omega}_{l,n}, \widehat{\mathbf{R}}_l^{(t)} \right) = \boldsymbol{\Psi}_{l,n}^{(t)} + \mathbf{k}_{c,l}^{(t)}(n) \mathbf{k}_{c,l}^{(t),H}(n). \quad (74)$$

Substituting (73) and (74) into (72) and then (71) yields (43). ■

REFERENCES

- [1] Y. Cui, F. Liu, X. Jing, and J. Mu, "Integrating sensing and communications for ubiquitous iot: Applications, trends and challenges," *arXiv preprint, arXiv:2104.11457*, 2021.
- [2] K. Chen, D. Zhang, L. Yao, B. Guo, Z. Yu, and Y. Liu, "Deep learning for sensor-based human activity recognition: Overview, challenges, and opportunities," *ACM Comput. Surv.*, vol. 54, no. 4, may 2021.
- [3] Q. Huang, H. Chen, and Q. Zhang, "Joint design of sensing and communication systems for smart homes," *IEEE Network*, vol. 34, no. 6, pp. 191–197, 2020.
- [4] A. Moreira, P. Prats-Iraola, M. Younis, G. Krieger, I. Hajnsek, and K. P. Papathanassiou, "A tutorial on synthetic aperture radar," *IEEE Geosci. Remote Sens. Mag.*, vol. 1, no. 1, pp. 6–43, 2013.
- [5] A. Zhang, M. L. Rahman, X. Huang, Y. J. Guo, S. Chen, and R. W. Heath, "Perceptive mobile networks: Cellular networks with radio vision via joint communication and radar sensing," *IEEE Veh. Technol. Mag.*, vol. 16, no. 2, pp. 20–30, 2021.
- [6] F. Liu, C. Masouros, A. P. Petropulu, H. Griffiths, and L. Hanzo, "Joint radar and communication design: Applications, state-of-the-art, and the road ahead," *IEEE Trans. Commun.*, vol. 68, no. 6, pp. 3834–3862, 2020.
- [7] F. Liu, Y. Cui, C. Masouros, J. Xu, T. X. Han, Y. C. Eldar, and S. Buzzi, "Integrated sensing and communications: Towards dual-functional wireless networks for 6g and beyond," *IEEE J. Sel. Areas Commun.*, pp. 1–1, 2022.
- [8] L. Xie, S. Song, Y. C. Eldar, and K. B. Letaief, "Collaborative sensing in perceptive mobile networks: Opportunities and challenges," *arXiv preprint arXiv:2205.15805*, 2022.
- [9] J. A. Zhang, F. Liu, C. Masouros, R. W. Heath, Z. Feng, L. Zheng, and A. Petropulu, "An overview of signal processing techniques for joint communication and radar sensing," *IEEE J. Sel. Top. Signal. Process.*, vol. 15, no. 6, pp. 1295–1315, 2021.
- [10] F. Liu, Y. Cui, C. Masouros, J. Xu, T. X. Han, Y. C. Eldar, and S. Buzzi, "Integrated sensing and communications: Towards dual-functional wireless networks for 6g and beyond," *arXiv preprint, arXiv:2108.07165*, 2021.
- [11] D. Bharadia, E. McMillin, and S. Katti, "Full duplex radios," in *Proceedings of the ACM SIGCOMM 2013 conference on SIGCOMM*, 2013, pp. 375–386.
- [12] A. Sabharwal, P. Schniter, D. Guo, D. W. Bliss, S. Rangarajan, and R. Wichman, "In-band full-duplex wireless: Challenges and opportunities," *IEEE J. Sel. Areas Commun.*, vol. 32, no. 9, pp. 1637–1652, 2014.

- [13] F. Dong, F. Liu, Y. Cui, W. Wang, K. Han, and Z. Wang, "Sensing as a service in 6g perceptive networks: A unified framework for isac resource allocation," *arXiv preprint arXiv:2202.09969*, 2022.
- [14] X. Wang, Z. Fei, J. A. Zhang, J. Huang, and J. Yuan, "Constrained utility maximization in dual-functional radar-communication multi-uav networks," *IEEE Trans. Commun.*, vol. 69, no. 4, pp. 2660–2672, 2021.
- [15] L. Xie, P. Wang, S. Song, and K. B. Letaief, "Perceptive mobile network with distributed target monitoring terminals: Leaking communication energy for sensing," *IEEE Trans. Wirel. Commun.*, vol. 21, no. 12, pp. 10193–10207, Dec. 2022.
- [16] W. L. Melvin, "A STAP overview," *IEEE Aerosp. Electron. Syst. Mag.*, vol. 19, no. 1, pp. 19–35, Jan 2004.
- [17] I. S. Reed, J. D. Mallett, and L. E. Brennan, "Rapid Convergence Rate in Adaptive Arrays," *IEEE Trans. Aerosp. Electron. Syst.*, vol. AES-10, no. 6, pp. 853–863, Nov 1974.
- [18] M. L. Rahman, J. A. Zhang, X. Huang, Y. J. Guo, and R. W. Heath, "Framework for a perceptive mobile network using joint communication and radar sensing," *IEEE Trans. Aerosp. Electron. Syst.*, vol. 56, no. 3, pp. 1926–1941, 2020.
- [19] S. Wang, Y. Hou, F. Gao, and X. Ji, "A novel iot access architecture for vehicle monitoring system," in *2016 IEEE 3rd World Forum on Internet of Things (WF-IoT)*, 2016, pp. 639–642.
- [20] S. Sun, A. P. Petropulu, and W. U. Bajwa, "Target estimation in colocated mimo radar via matrix completion," in *2013 IEEE International Conference on Acoustics, Speech and Signal Processing*. IEEE, 2013, pp. 4144–4148.
- [21] S. Sun, W. U. Bajwa, and A. P. Petropulu, "Mimo-mc radar: A mimo radar approach based on matrix completion," *IEEE Trans. Aerosp. Electron. Syst.*, vol. 51, no. 3, pp. 1839–1852, 2015.
- [22] B. Li, A. P. Petropulu, and W. Trappe, "Optimum co-design for spectrum sharing between matrix completion based mimo radars and a mimo communication system," *IEEE Trans. Signal Process.*, vol. 64, no. 17, pp. 4562–4575, 2016.
- [23] R. Boyer, "Performance bounds and angular resolution limit for the moving colocated mimo radar," *IEEE Transactions on Signal Processing*, vol. 59, no. 4, pp. 1539–1552, 2011.
- [24] S. Sun, A. P. Petropulu, and H. V. Poor, "Mimo radar for advanced driver-assistance systems and autonomous driving: Advantages and challenges," *IEEE Signal Processing Magazine*, vol. 37, no. 4, pp. 98–117, 2020.
- [25] L. Xie, Z. He, J. Tong, and W. Zhang, "A recursive angle-doppler channel selection method for reduced-dimension space-time adaptive processing," *IEEE Trans. Aerosp. Electron. Syst.*, vol. 56, no. 5, pp. 3985–4000, 2020.
- [26] M. Liu, L. Zou, X. Yu, Y. Zhou, X. Wang, and B. Tang, "Knowledge aided covariance matrix estimation via gaussian kernel function for airborne sr-stap," *IEEE Access*, vol. 8, pp. 5970–5978, 2020.
- [27] Y. Wu, T. Wang, J. Wu, and J. Duan, "Training sample selection for space-time adaptive processing in heterogeneous environments," *IEEE Geosci. Remote. Sens. Lett.*, vol. 12, no. 4, pp. 691–695, 2015.
- [28] E. Fishler, A. Haimovich, R. Blum, D. Chizhik, L. Cimini, and R. Valenzuela, "Mimo radar: an idea whose time has come," in *Proceedings of the 2004 IEEE Radar Conference (IEEE Cat. No.04CH37509)*, 2004, pp. 71–78.
- [29] B. Friedlander, "On signal models for mimo radar," *IEEE Trans. Aerosp. Electron. Syst.*, vol. 48, no. 4, pp. 3655–3660, 2012.
- [30] M. Z. Win and J. H. Winters, "Analysis of hybrid selection/maximal-ratio combining in rayleigh fading," in *1999 IEEE International Conference on Communications (Cat. No. 99CH36311)*, vol. 1. IEEE, 1999, pp. 6–10.
- [31] A. Wiesel, Y. C. Eldar, and S. Shamai, "Zero-forcing precoding and generalized inverses," *IEEE Transactions on Signal Processing*, vol. 56, no. 9, pp. 4409–4418, 2008.
- [32] M. R. Akdeniz, Y. Liu, M. K. Samimi, S. Sun, S. Rangan, T. S. Rappaport, and E. Erkip, "Millimeter wave channel modeling and cellular capacity evaluation," *IEEE J. Sel. Areas Commun.*, vol. 32, no. 6, pp. 1164–1179, 2014.
- [33] F. Robey, D. Fuhrmann, E. Kelly, and R. Nitzberg, "A cfar adaptive matched filter detector," *IEEE Trans. Aerosp. Electron. Syst.*, vol. 28, no. 1, pp. 208–216, 1992.

- [34] E. J. Kelly and K. M. Forsythe, "Adaptive detection and parameter estimation for multidimensional signal models," Massachusetts Inst of Tech Lexington Lincoln Lab, Tech. Rep., 1989.
- [35] D. Shnidman, "The calculation of the probability of detection and the generalized marcum q-function," *IEEE Trans. Inf. Theory*, vol. 35, no. 2, pp. 389–400, 1989.
- [36] J. Omura and T. Kailath, "Some useful probability distributions," STANFORD UNIV CA STANFORD ELECTRONICS LABS, Tech. Rep., 1965.
- [37] A. P. Dempster, N. M. Laird, and D. B. Rubin, "Maximum likelihood from incomplete data via the em algorithm," *J. R. Stat. Soc. Series B Stat. (Methodol.)*, vol. 39, no. 1, pp. 1–22, 1977.
- [38] C. M. Bishop and N. M. Nasrabadi, *Pattern recognition and machine learning*. Springer, 2006, vol. 4, no. 4.
- [39] L. Xie, Z. He, J. Tong, T. Liu, J. Li, and J. Xi, "Regularized covariance estimation for polarization radar detection in compound gaussian sea clutter," *IEEE Trans. Geosci. Remote Sens.*, vol. 60, pp. 1–16, 2022.
- [40] Y. Chen, A. Wiesel, Y. C. Eldar, and A. O. Hero, "Shrinkage algorithms for mmse covariance estimation," *IEEE Trans. Signal Process.*, vol. 58, no. 10, pp. 5016–5029, 2010.
- [41] J. Ma and L. Ping, "Orthogonal amp," *IEEE Access*, vol. 5, pp. 2020–2033, 2017.
- [42] M. R. Akdeniz, Y. Liu, M. K. Samimi, S. Sun, S. Rangan, T. S. Rappaport, and E. Erkip, "Millimeter wave channel modeling and cellular capacity evaluation," *IEEE J. Sel. Areas Commun.*, vol. 32, no. 6, pp. 1164–1179, 2014.
- [43] Y. Sun, Á. Baricz, and S. Zhou, "On the monotonicity, log-concavity, and tight bounds of the generalized marcum and nuttall q -functions," *IEEE Trans. Inf. Theory*, vol. 56, no. 3, pp. 1166–1186, 2010.
- [44] Y. Sun and Á. Baricz, "Inequalities for the generalized marcum q -function," *Appl. Math. Comput.*, vol. 203, no. 1, pp. 134–141, 2008.
- [45] P. Sahoo and T. Riedel, *Mean value theorems and functional equations*. World Scientific, 1998.
- [46] S. M. Kay, *Fundamentals of statistical signal processing: estimation theory*. Prentice-Hall, Inc., 1993.